**Development and evaluation of the interactive Model for Air Pollution and Land**

**Ecosystems (iMAPLE) version 1.0**

Xu Yue[1#], Hao Zhou[2,3#], Chenguang Tian[1], Yimian Ma[4], Yihan Hu[1], Cheng Gong[4], Hui Zheng[5], Hong Liao[1]

[1]Jiangsu Key Laboratory of Atmospheric Environment Monitoring and Pollution Control, Collaborative Innovation Center of Atmospheric Environment and Equipment Technology, School of Environmental Science and Engineering, Nanjing University of Information Science & Technology (NUIST), Nanjing, 210044, China
[2]College of Meteorology and Oceanography, National University of Defense Technology, Changsha, 410073, China
[3]High Impact Weather Key Laboratory of China Meteorological Administration (CMA), Changsha, 410073, China
[4] Department Biogeochemical Integration, Max Planck Institute for Biogeochemistry, Jena, 07745, Germany
[5] Key Laboratory of Regional Climate-Environment Research for Temperate East Asia, Institute of Atmospheric Physics, Chinese Academy of Sciences, Beijing, 100029, China

Corresponding authors: Xu Yue (yuexu@nuist.edu.cn)

[#] These authors contributed equally

**Abstract**

Land ecosystems are important sources and sinks of atmospheric components. In turn, air pollutants affect the exchange rates of carbon and water fluxes between ecosystems and atmosphere. However, these biogeochemical processes are usually not well presented in the Earth system models, limiting the explorations of interactions between land ecosystems and air pollutants from the regional to global scales. Here, we develop and validate the interactive Model for Air Pollution and Land Ecosystems (iMAPLE) by upgrading the Yale Interactive terrestrial Biosphere model with process-based water cycles, fire emissions, wetland methane ($CH_4$) emissions, and the trait-based ozone ($O_3$) damages. Within the iMAPLE, soil moisture and temperature are dynamically calculated based on the water and energy balance in soil layers. Fire emissions are dependent on dryness, lightning, population, and fuel load. Wetland $CH_4$ is produced but consumed through oxidation, ebullition, diffusion, and plant-mediated transport. The trait-based scheme unifies $O_3$ sensitivity of different plant functional types (PFTs) with the leaf mass per area. Validations show correlation coefficients ($R$) of 0.59-0.86 for gross primary productivity (GPP) and 0.57-0.84 for evapotranspiration (ET) across the six PFTs at 201 flux tower sites, and yield an average $R$ of 0.68 for $CH_4$ emissions at 44 sites. Simulated soil moisture and temperature match reanalysis data with the high $R$ above 0.86 and low normalized mean biases (NMB) within 7%, leading to reasonable simulations of global GPP ($R$=0.92, NMB=1.3%) and ET ($R$=0.93, NMB=-10.4%) against satellite-based observations for 2001-2013. The model predicts an annual global area burned of 507.1 Mha, close to the observations of 475.4 Mha with a spatial $R$ of 0.66 for 1997-2016. The wetland $CH_4$ emissions are estimated to be 153.45 Tg [$CH_4$] $yr^{-1}$ during 2000-2014, close to the multi-model mean of 148 Tg [$CH_4$] $yr^{-1}$. The model also shows reasonable responses of GPP and ET to the changes in diffuse radiation, and yields a mean $O_3$ damage of 2.9% to global GPP. The iMAPLE model provides an advanced tool for studying the interactions between land ecosystem and air pollutants.

**Keywords:** carbon fluxes, water cycle, fire emissions, methane emissions, ozone damage, diffuse radiation.

## 1. Introduction

As an important component on the Earth, land ecosystems regulate global carbon and water cycles. Every year, the terrestrial ecosystem assimilates ~120 Pg (1 Pg = $10^{15}$ g) carbon from atmosphere through vegetation photosynthesis (Beer et al., 2010). However, most of this carbon uptake returns to atmosphere due to plant and soil respiration (Sitch et al., 2015), as well as other perturbations such as biomass burning and biogenic emissions (van der Werf et al., 2010;Carslaw et al., 2010), leading to a net carbon sink of only ~2 Pg C $yr^{-1}$ during 1960-2021 (Friedlingstein et al., 2022). Meanwhile, land ecosystems affect atmospheric moisture and soil wetness through both physical (e.g., evaporation and runoff) and physiological (e.g., leaf transpiration and root hydrological uptake) processes. Observations show that transpiration accounts for 80%-90% of the terrestrial evapotranspiration (ET) (Jasechko et al., 2013) and makes significant contributions to land precipitation especially over the tropical forests (Spracklen et al., 2012).

Different approaches have been applied to depict the spatiotemporal variations of ecosystem processes. The eddy covariance technique provides direct measurements of land carbon and water fluxes (Jung et al., 2011). However, the limited number and uneven distribution of ground sites results in large uncertainties in the upscaling of site-level fluxes to the global scale (Jung et al., 2020b). Satellite retrieval provides a unique tool for the continuous representations of land fluxes in both space and time (Worden et al., 2021). However, most of the ecosystem variables (e.g., gross primary productivity, GPP) can only be derived using available signals from remote sensing through empirical relationships (Madani et al., 2017). As a comparison, process-based models build physical parameterizations based on field and/or laboratory experiments and validate against the available *in situ* and satellite-based observations (Niu et al., 2011;Castillo et al., 2012). These models can be further applied at different spatial (from site to global) and temporal (from days to centuries) scales to identify the main drivers of the changes in carbon and water fluxes (Sitch et al., 2015). For example, a total of

17 vegetation models were validated and combined to predict the land carbon fluxes in the past century (Friedlingstein et al., 2022); the ensemble mean of these models revealed a steadily increasing land carbon sink from 1960 with the dominant contribution by $CO_2$ fertilization.

While many studies quantified the ecosystem responses to the effects of $CO_2$, climate, and human activities (Piao et al., 2009;Sitch et al., 2015), few have explored the interactions between air pollution and land ecosystems. Such biogeochemical processes become increasingly important in the Anthropocene period with significant changes in atmospheric compositions. For example, observations found that nitrogen and phosphorus constrain the $CO_2$ fertilization efficiency of global vegetation (Terrer et al., 2019), but such limiting effect is ignored or underestimated in most of the current models (Wang et al., 2020). Tropospheric ozone ($O_3$) damages plant photosynthesis and stomatal conductance, inhibiting carbon assimilation and the ET from the land surface (Sitch et al., 2007;Lombardozzi et al., 2015). Atmospheric aerosols can enhance photosynthesis through diffuse fertilization effects (Mercado et al., 2009) but meanwhile decrease photosynthesis by reducing precipitation (Yue et al., 2017). In turn, ecosystems act as both the sources and sinks of atmospheric components. Biomass burning emits a large amount of carbon dioxide, trace gases, and particulate matter, further influencing air quality (Chen et al., 2021), ecosystem functions (Yue and Unger, 2018), and global climate (Tian et al., 2022). Biogenic volatile organic compounds (BVOCs) are important precursors for both surface $O_3$ and secondary organic aerosols (Wu et al., 2020), which can feed back to affect biogenic emissions (Yuan et al., 2016) and carbon assimilation (Rap et al., 2018). Wetland methane ($CH_4$) emissions account for the dominant fraction of natural sources of $CH_4$, and are projected to increase under the global warming scenarios (Rosentreter et al., 2021;Zhang et al., 2017). On the other hand, stomatal uptake dominates the dry deposition of air pollutants over the vegetated land (Lin et al., 2020). Meanwhile, ET from forest results in the increase of water vapor in atmosphere (Spracklen et al., 2012), affecting the consequent rainfall and wet

115  deposition of particles.

116

117  Currently, numerical models are in general developed separately for atmospheric

118  chemistry and ecosystem processes. The chemical transport models are usually driven

119  with prescribed emissions of biomass burning (Warneke et al., 2023) and wetland

120  methane (Heimann et al., 2020), while the ecosystem models often ignore the

121  biogeochemical impacts of $O_3$ and aerosols (Friedlingstein et al., 2022). In an earlier

122  study, we developed and validated the Yale Interactive terrestrial Biosphere (YIBs)

123  model version 1.0 with the special focus on the interactions between atmospheric

124  chemistry and land ecosystems (Yue and Unger, 2015). Thereafter, the YIBs model has

125  been used offline to assess the $O_3$ vegetation damage (Yue et al., 2016), aerosol diffuse

126  fertilization (Yue and Unger, 2017), BVOC emissions (Cao et al., 2021a), as well as

127  coupled to other models to investigate the carbon-chemistry-climate interactions (Lei

128  et al., 2020;Gong et al., 2021). The YIBs model has joined the multi-model

129  intercomparison project of TRENDY since the year 2020 and showed reasonable

130  performance in the simulation of carbon fluxes (Friedlingstein et al., 2020). However,

131  the YIBs model failed to predict the typical hydrological variables such as ET and

132  runoff due to the missing of carbon-water coupling modules. Furthermore, the model

133  did not consider the nutrient limitation on plant photosynthesis and ignored some key

134  exchange fluxes between land and atmosphere.

135

136  In this study, we develop the interactive Model for Air Pollution and Land Ecosystems

137  (iMAPLE) by coupling the process-based water cycle module from Noah-MP (Niu et

138  al., 2011) to the carbon cycle in the YIBs (Figure 1). In addition, we update the original

139  YIBs model with some major advances in the biogeochemical processes including

140  dynamic fire emissions, wetland $CH_4$ emissions, nutrient limitations on photosynthesis,

141  and the trait-based $O_3$ vegetation damage. The detailed descriptions of these updates

142  are presented in the next section. The iMAPLE model is fully validated against

143  available measurements in Section 3. The last section will summarize the model

144    performance and rethink the prospective directions for future development.

145

146    **2. Models and data**

147    **2.1 Main features of YIBs model**

148    The YIBs model is a process-based vegetation model predicting land carbon fluxes with

149    dynamic changes in tree height, leaf area index, and carbon pools (Yue and Unger, 2015,

150    thereafter YU2015). A total of nine plant functional types (PFTs) are considered

151    including evergreen broadleaf forest (EBF), evergreen needleleaf forest (ENF),

152    deciduous broadleaf forest (DBF), tundra, shrubland, $C_3/C_4$ grassland, and $C_3/C_4$

153    cropland. At each gridbox, a mixture of PFTs with each PFT fraction is used as model

154    input, sharing the temperature or moisture information from the same soil column. Leaf

155    photosynthesis is calculated using the well-established Michaelis-Menten enzyme-

156    kinetics scheme (Farquhar et al., 1980) and is coupled to stomatal conductance with the

157    modulations of air humidity and $CO_2$ concentrations (Ball et al., 1987). The model

158    applies a two-leaf approach to distinguish the irradiating states for sunlit and shading

159    leaves and adopts an adaptive stratification for the radiative transfer processes within

160    canopy layers (Spitters, 1986). The gross carbon assimilation is further regulated by the

161    optimized plant phenology, which is mainly dependent on temperature and light for

162    deciduous trees (Yue et al., 2015) but temperature and/or moisture for shrubland and

163    grassland (YU2015). The assimilated carbon is allocated among leaf, stem, and root to

164    support autotrophic respiration and development, the latter of which is used to update

165    plant height and leaf area (Cox, 2001). The input of litterfall triggers the carbon

166    transition among 12 soil carbon pools and determines the magnitude of heterotrophic

167    respiration with the joint effects of soil temperature, moisture, and texture (Schaefer et

168    al., 2008). The net carbon uptake is then calculated by subtracting ecosystem respiration

169    (plant and soil) and environmental perturbations (reforestation or deforestation) from

170    the gross carbon assimilation (Yue et al., 2021). The YIBs model reasonably reproduces

171    the observed spatiotemporal patterns of global carbon fluxes and makes contributions

172    to the Global Carbon Project with the long-term simulations of land carbon sink in the

past century (Friedlingstein et al., 2020). The model specifically considers air pollution impacts on land ecosystems (Figure 1), such as the ozone vegetation damage (Yue and Unger, 2014) and aerosol diffuse fertilization effect (Yue and Unger, 2017). The YIBs implements two different schemes for BVOCs emissions (Figure 1), including the Model of Emissions of Gases and Aerosols from Nature (MEGAN, Guenther et al., 2012) and the photosynthesis-dependent (PS_BVOC) scheme (Unger et al., 2013).

## 2.2 New processes in the iMAPLE model

2.2.1 Process-based water cycles

The descriptions and units of all parameters used in this study are shown in Table S1. We implement the hydrological module from Noah-MP into the iMAPLE model (Niu et al., 2011). The water budget closure is achieved by constructing water-balance equations among precipitation ($P$, Kg m$^{-2}$ s$^{-1}$), evapotranspiration ($ET$, Kg m$^{-2}$ s$^{-1}$), runoff, and terrestrial water storage change ($\Delta TWS$) on each grid cell as follows:

$$P = ET + runoff + \Delta TWS \qquad (1)$$

Here, hourly $P$ from MERRA-2 reanalyses is used as the input.

We then divide $ET$ into three portions including plant transpiration ($TRA$), canopy evaporation ($ECAN$) and ground evaporation ($EGRO$):

$$ET = TRA + ECAN + EGRO \qquad (2)$$

For vegetated grids, $TRA$ is calculated as follows:

$$TRA = \frac{\rho_{air} \cdot CP_{air} \cdot C_{tra} \cdot (e_{sat} - e_{ca})}{PC} \qquad (3)$$

where $\rho_{air}$ is air density, $CP_{air}$ is heat capacity of dry air, and $PC$ is the psychrometric constant. $e_{sat}$ is the saturated vapor pressure at the leaf temperature, $e_{ca}$ is the vapor pressure of the canopy air and $C_{tra}$ is leaf transpiration conductance, which is calculated based on the Ball-Berry scheme of stomatal resistance (Yue and Unger, 2015). Meanwhile, $ECAN$ is calculated as follows:

$$ECAN = \frac{\rho_{air} \cdot CP_{air} \cdot C_{canopy,evap} \cdot (e_{sat} - e_{ca})}{PC} \qquad (4)$$

$$C_{canopy,evap} = \frac{f_{wet} \cdot E_{VAI}}{R_{leaf,bdy}} \qquad (5)$$

Here, $C_{canopy,evap}$ is the latent heat conductance from the wet leaf surface to canopy air. $f_{wet}$ is the wet fraction of canopy, which is a fraction of the maximum canopy precipitation interception capacity. $E_{VAI}$ is the effective vegetation area index and $R_{leaf,bdy}$ is the bulk leaf boundary resistance. $EGRO$ is calculated as follows:

$$EGRO = C_{ground,evap}(e_{sat,ground} RH - e_{ca}) \qquad (6)$$

Here, $C_{ground,evap}$ is the coefficient for latent heat at the ground, $e_{sat,ground}$ is the saturated vapor pressure at the ground and RH is the surface relative humidity.

Runoff includes surface ($R_{srf}$) and subsurface ($R_{sub}$) components:

$$runoff = R_{srf} + R_{sub} \qquad (7)$$

The surface runoff is calculated as follows:

$$R_{srf} = Q_{soil,srf} - Q_{soil,in} \qquad (8)$$

where $Q_{soil,srf}$ is the incident water in the soil surface and is the sum of the precipitation, snowmelt and dewfall. $Q_{soil,in}$ is the infiltration into the soil, which is derived from approximate solutions of Richards equations with considerations of the spatial variations in precipitation and infiltration capacity. Here, we assume exponential distributions of infiltration capacity in each grid cell following the approach by Schaake et al. (1996):

$$Q_{soil,in} = Q_{soil,srf} \frac{I_c}{Q_{soil,srf}\Delta t + I_c} \qquad (9)$$

$$I_c = W_d[1 - \exp(-K_{\Delta t}\Delta t)] \qquad (10)$$

Here, $I_c$ and $W_d$ are the soil infiltration capacity of the model grid cell and the water deficit of the soil column, respectively. $K_{\Delta t}$ and $\Delta t$ are the calibratable parameters and model time step. We assume free drainage processes in the soil column bottom, thus the $R_{sub}$ is calculated as follows:

$$R_{sub} = \alpha_{slope} \cdot K_4 \qquad (11)$$

where $\alpha_{slope} = 0.1$ is the terrain slope index. $K_4$ is the hydraulic conductivity in the bottom soil layer parameterized following the scheme in Clapp and Hornberger (1978) and is calculated using spatial soil profiles from Hengl et al. (2017).

230

Terrestrial water storage (*TWS*) is the sum of groundwater storage ($W_{gw}$), soil water

content ($W_{soil}$) and snow water equivalent ($W_{snow}$):

$$TWS = W_{gw} + W_{snow} + \sum_{i=1}^{N_{soil}} W_{soil} \tag{12}$$

Here, the soil module includes four layers ($N_{soil} = 4$) and $W_{soil}$ is calculated by the

volumetric water content ($W_i$) as follows:

$$W_{soil} = \rho_{wat} \cdot W_i \cdot \Delta Z_i \quad for \ i = 1, 2, 3, 4 \tag{13}$$

where water density ($\rho_{wat}$) = 1000 kg m$^{-3}$, and $\Delta Z_i$ = 0.1, 0.3, 0.6 and 1m, respectively.

Hourly $W_i$ depends on variations of soil water diffusion ($D$) and hydraulic conductivity

($K$) as follows:

$$\frac{\partial W}{\partial t} = \frac{\partial}{\partial z}\left(D \frac{\partial W}{\partial z}\right) + \frac{\partial K}{\partial z} \tag{14}$$

Here, $K$ and $D$ are calculated following the parameterizations of Clapp-Hornberger

curves (Clapp and Hornberger, 1978):

$$\frac{K}{K_{sat}} = \left(\frac{W}{W_{sat}}\right)^{2b+3} \tag{15}$$

$$D = K \cdot \frac{\partial \varphi}{\partial W} \tag{16}$$

$$\frac{\varphi}{\varphi_{sat}} = \left(\frac{W}{W_{sat}}\right)^{-b} \tag{17}$$

where $\varphi_{sat}$, $W_{sat}$ and $K_{sat}$ are saturated soil capillary potential, volumetric water

content and hydraulic conductivity. Exponent $b$ is an empirical constant depending

on soil types. Soil moisture is calculated as the ratio of $W_s$ to $W_{sat}$.

Soil temperature ($T_s$) is calculated through physical processes as follows:

$$\frac{\partial T_s}{\partial t} = \frac{1}{C}\frac{\partial}{\partial z}\left(K_T \frac{\partial T_s}{\partial z}\right) \tag{18}$$

Here $K_T$ is soil specific heat capacity:

$$K_T = K_e \cdot \left(K_s - K_{dry}\right) + K_{dry} \tag{19}$$

where $K_e$, $K_s$ and $K_{dry}$ are Kersten values as a function of soil wetness, saturated soil

heat conductivity and that under dry air conditions (Niu et al., 2011). $C$ in Equation (13)

256 is the specific heat

$$C = W_{lip} \cdot C_{lip} + W_{ice} \cdot C_{ice} + (1 - W_{sat}) \cdot C_{sat} + (W_{sat} - W) \cdot C_{air} \quad (20)$$

258 Here, $W_{lip}$, $C_{lip}$ and $W_{ice}$, $C_{ice}$ indicate water content and heat capacity on soil water

259 and ice. $C_{sat}$ and $C_{air}$ are saturated and air heat capacity, which are empirical constants

260 (Niu et al., 2011).

261

262 2.2.2 Dynamic fire emissions

263 We implement the active global fire parameterizations from Pechony and Shindell

264 (2009) and Li et al. (2012) to the iMAPLE model. The fire emissions are determined

265 by several key factors such as fuel flammability, natural ignitions, human activities, and

266 fire spread. The fire count $N_{fire}$ depends on flammability (*Flam*), fire ignition (including

267 both natural ignition rate $I_N$ and anthropogenic ignition rate $I_A$ and anthropogenic

268 suppression ($F_{NS}$):

$$N_{fire} = Flam \times (I_N + I_A) \times F_{NS} \quad (21)$$

270 *Flam* is a unitless metric representing conditions conducive to fire occurrence. It is

271 parameterized as a function of vapor pressure deficit (VPD), precipitation (Prec), and

272 leaf area index (LAI):

$$Flam = VPD \times e^{-2 \times Prec} \times LAI \quad (22)$$

274 $I_N$ depends on the cloud-to-ground lightning and $I_A$ can be expressed as:

$$I_A = 0.03 \times PD \times k(PD) \quad (23)$$

276 where *PD* is population density. The empirical function of $k(PD) = 6.8 \times PD^{-0.6}$ stands

277 for ignition potentials by human activity. The fraction of non-suppressed fires $F_{NS}$ is

278 derived as:

$$F_{NS} = 0.05 + 0.95 \times e^{-0.05 \times PD} \quad (24)$$

280

281 The burned area of a single fire (*BA*$_{single}$) is typically taken to be elliptical in shape

282 associated with length-to-breadth ratio (*LB*), head-to-back ratio (HB) and rate of fire

283 spread (*UP*) as follows:

$$BA_{single} = \frac{\pi \times UP^2}{4 \times LB} \times (1 + \frac{1}{HB})^2 \quad (25)$$

285    Then, LB and HB are related to changes of near-surface wind speed ($U$) as follows:

286
$$LB = 1 + 10 \times (1 - e^{-0.06 \times U}) \tag{26}$$

287
$$HB = \frac{LB + (LB^2 - 1)^{0.5}}{LB - (LB^2 - 1)^{0.5}} \tag{27}$$

288    Meanwhile, $UP$ is computed as the function of relative humidity ($RH$):

289
$$UP = UP_{max} \times f_{RH} \times f_\theta \times G(W) \tag{28}$$

290    Here, $UP_{max}$ is the maximum fire spread rate depending on PFTs, $f_{RH}$ and $f_\theta$ represent

291    the dependence of fire spread on RH and on root-zone soil moisture, respectively. $f_\theta$ is

292    simply set to 0.5 and $f_{RH}$ is calculated as:

293
$$f_{RH} = \begin{cases} 1, & RH \leq RH_{low} \\ \frac{RH - RH_{low}}{RH_{up} - RH_{low}}, & RH_{low} < RH < RH_{up} \\ 0, & RH \geq RH_{up} \end{cases} \tag{29}$$

294    In this study, we set $RH_{low}$ =30 % and $RH_{up}$ =70 % as the lower and upper thresholds of

295    $RH$ following the methods used in Li et al. (2012). If $RH$ is higher than 70%, natural

296    fires will not occur or spread, and RH will no longer be a constraint for fire occurrence

297    and spread if $RH \leq 30\%$. G(W) is the limit of the fire spread:

298
$$G(W) = \frac{LB}{1 + \frac{1}{HB}} \tag{30}$$

299    In general, the eccentricity of burned area is primarily influenced by near-surface wind

300    speed, while the rate of fire spread is jointly regulated by near-surface wind speed and

301    relative humidity. The shape of the fire is converted to a circular form when the near-

302    surface wind speed reaches zero, and burning ceases to propagate once the relative

303    humidity is above a specific threshold. The dependence of $BA_{single}$ on $U$ and $RH$ is

304    shown in Figure S1.

305

306    Finally, the burned aera ($BA$) is represented as:

307
$$BA = BA_{single} \times N_{fire} \tag{31}$$

308    The fire-emitted trace gases and aerosols ($Emis$) are calculated as:

309
$$Emis = BA \times EF \tag{32}$$

310    where $EF$ is the emission factors for different species (such as black carbon and organic

311    carbon aerosols). It is important to note that the feedbacks from fire activities onto the

terrestrial ecosystem have not been considered in the current version of the iMAPLE model due to the high complexity.

### 2.2.3 Wetland methane emissions

We implement the process-based wetland $CH_4$ emissions into the iMAPLE model. The anthropogenic sources of $CH_4$ from Phase 6 of the Coupled Model Intercomparison Project (CMIP6, https://esgf-node.llnl.gov/projects/input4mips/) are also used as input for iMAPLE. For each soil layer, the flux of $CH_4$ ($F_{CH_4}$) is calculated as the difference between production ($P_{CH_4}$) and consumptions, which include oxidation ($O_{CH_4}$), ebullition ($E_{CH_4}$), diffusion ($D_{CH_4}$), and plant-mediated transport through aerenchyma ($A_{CH_4}$) as follows:

$$F_{CH_4} = P_{CH_4} - O_{CH_4} - E_{CH_4} - D_{CH_4} - A_{CH_4} \tag{33}$$

The net methane emission to the atmosphere is the sum of ebullition, diffusion and aerenchyma transport from the top soil layer.

The production of $CH_4$ in soil depends on the quantity of carbon substrate and environmental conditions including soil temperature $T_s$, pH, and wetland inundation fraction $f_{wetland}$ as follows:

$$P_{CH_4} = R_h r f_{Ts} f_{pH} f_{wetland} \tag{34}$$

where $R_h$ is the heterotrophic respiration estimated at the grid cell ($mol\ C\ m^{-2}\ s^{-1}$). $r$ represents the release ratio of methane and carbon dioxide (Wania et al., 2010). We determine the dependence on $T_s$ and soil pH in iMAPLE based on the parameterizations from the TRIPLEX-GHG model (Zhu et al., 2014). The impact factor of soil temperature $f_{ST}$ can be calculated as follows (Zhang et al., 2002; Zhu et al., 2014):

$$f_{ST} = \begin{cases} 0, & T_s < T_{min} \\ vt^{xt} \exp\big(xt(1 - vt)\big), & T_{min} \leq T_s \leq T_{max} \\ 0, & T_s > T_{max} \end{cases} \tag{35}$$

$$vt = (T_{max} - T_s)/(T_{max} - T_{opt}) \tag{36}$$

$$xt = \big[\log(Q_{10})\,(T_{max} - T_{opt})\big]^2 (1.0 + at^{0.5})^2/400.0 \tag{37}$$

$$at = 1.0 + 40.0/[\log(Q_{10})(T_{max} - T_{opt})] \tag{38}$$

$T_{min}$, $T_{max}$, and $T_{opt}$ represents the lowest, highest and optimum temperature for the process of methane production and oxidation, respectively. In this study, the $T_{min} = 0°C$, $T_{max} = 45°C$ and $T_{opt} = 25°C$ (Zhu et al., 2014).

For the temperature-dependence, the $Q_{10}$ relationships are applied as follows:

$$Q_{10} = r_b Q_b^{\frac{T_s - T_{base}}{10}} \tag{39}$$

Here $r_b$ is set to 3.0 and $Q_b$ is 1.33 with a base temperature ($T_{base}$) of 25°C (Zhu et al., 2014;Paudel et al., 2016). The inundation fraction of wetland at each cell describes the proportion of anaerobic conditions (Zhang et al., 2021). We ignore the impact of redox potential (Eh) because global observations are not available and the Eh-related processes are poorly characterized in current models (Wania et al., 2010).

The oxidation of CH4 is a series of aerobic activities related to temperature and CH4 concentrations:

$$O_{CH_4} = [CH_4] f_{Ts} f_{CH_4} \tag{40}$$

where $[CH_4]$ is the methane amount in each soil layer ($gCm^{-2}layer^{-1}$). $f_{CH4}$ is the CH4 concentration factor representing a Michaelis-Menten kinetic relationship:

$$f_{CH4} = \frac{[CH_4]}{[CH_4] + K_{CH4}} \tag{41}$$

where $K_{CH4} = 5 \ \mu mol \ L^{-1}$ is the half-saturation coefficient with respect to CH4 (Walter and Heimann, 2000). For temperature-dependence of oxidation, the $Q_{10}$ relationship with $r_b = 2.0$, $Q_b = 1.9$, and $T_{base} = 12°C$ is adopted (Zhu et al., 2014;Paudel et al., 2016).

The diffusion of CH4 follows the Fick's law with dependence on CH4 concentrations and the molecular diffusion coefficients of CH4 in the air ($D_a = 0.2 \ cm^2 s^{-1}$) and water ($D_w = 0.00002 \ cm^2 s^{-1}$) respectively (Walter and Heimann, 2000). For each soil layer $i$, the diffusion coefficient $D_i$ can be calculated as follows :

$$D_i = D_a \times (R_{sand} \times 0.45 + R_{silt} \times 0.2 + R_{clay} \times 0.14) \times f_{tort} \times S_{poro} \times (1 - WFPS_i) + D_w \times WFPS_i \tag{42}$$

where $R_{sand}$, $R_{silt}$, $R_{clay}$ is the relative content of sand, silt, and clay in the soil, $f_{tort} = 0.66$ is tortuosity coefficient, $S_{poro}$ is soil porosity, and $WFPS$ represents the pore space full of water (Zhuang et al., 2004).

The ebullition of $CH_4$ occurs when $CH_4$ concentration is above the threshold of 0.5 $mol\ CH_4 m^{-3}$ (Walter et al., 2001). Since the process of ebullition occurs in a very short time, the bubbles will generate at once and all the flux will be released to atmosphere if the concentration reaches the threshold. The plant-mediated transport of $CH_4$ through aerenchyma is dependent on the concentration gradient of $CH_4$ and plant-related factors (Zhu et al., 2014). The $A_{CH_4}$ is determined by the oxidation factor for roots and the aerenchyma factor for plants. The baseline value of the oxidation factor in roots is 0.5, with a regulatory range from 0.2 to 1.0 determined by the wetland plant types. The plant aerenchyma factor is calculated by the ratio of the plant root length density (typical value: 2.1 cm mg$^{-1}$) and the root cross-sectional area (typical value: 0.0013 cm$^2$), along with a plant root to atmosphere diffusion factor for methane which is modulated by plant type within a range of 0 to 1 (Zhang et al., 2002).

2.2.4 The down regulation on photosynthesis

We implement the down regulation parameterization from Arora et al. (2009) to indicate the nutrient limitations on leaf photosynthesis. A down-regulating factor $\varepsilon$ is calculated as a function of $CO_2$ concentrations ($C$) as follows:

$$\varepsilon(C) = \frac{1+\gamma_{gd}\ln{(C/C_0)}}{1+\gamma_g\ln{(C/C_0)}} \tag{43}$$

where $C_0$ is a reference $CO_2$ concentration set to 288 ppm. The values of $\gamma_{gd} = 0.42$ and $\gamma_g=0.90$ are derived from multiple measurements to constrain the $CO_2$ fertilization. Then the down-regulated photosynthesis is calculated by scaling the original value with the factor of $\varepsilon$.

2.2.5 Trait-based $O_3$ vegetation damaging scheme

The YIBs model considers $O_3$ vegetation damage using the flux-based scheme proposed

by Sitch et al. (2007) (thereafter S2007), which determines the damaging ratio $F$ of plant photosynthesis as follows:

$$F = a_{PFT} \times max\{f_{O3} - t_{PFT}, 0\} \tag{44}$$

Here, the $f_{O3}$ denotes $O_3$ stomatal flux (nmol m$^{-2}$ s$^{-1}$) defined as:

$$f_{O3} = \frac{[O_3]}{r + \left[\frac{k_{O3}}{g_p \times (1-F)}\right]} \tag{45}$$

where $[O_3]$ represents the $O_3$ concentrations at the reference level (nmol m$^{-3}$). $r$ is the sum of boundary and aerodynamic resistance between leaf surface and reference level (s m$^{-1}$). $g_p$ is the potential stomatal conductance for H$_2$O (m s$^{-1}$). $k_{O3} = 1.67$ is a conversion factor of leaf resistance for $O_3$ to that for water vapor. The level of $O_3$ damage is then determined by the PFT-specific sensitivity $a_{PFT}$ and threshold $t_{PFT}$, which are different among PFTs.

In iMAPLE, we implement the trait-based $O_3$ vegetation damaging scheme to unify the inter-PFT sensitivities (Ma et al., 2023):

$$a_{PFT} = \frac{a}{LMA} \tag{46}$$

Here, a unified plant sensitivity $a$ (nmol$^{-1}$ g s) is scaled by leaf mass per area (LMA, g m$^{-2}$) to derive the sensitivity of a specific PFT ($a_{PFT}$). Accordingly, the damaging fraction $F$ is modified as follows:

$$F = a \times max\left\{\frac{f_{O3}}{LMA} - t, 0\right\} \tag{47}$$

Here $t$ (nmol g$^{-1}$ s$^{-1}$) is a unified flux threshold for $O_3$ vegetation damage. The $f_{O3}$ in Equation (45) is fed into Equation (47) so as to build a quadratic equation for F. We solve the quadratic equation and select the $F$ value within the range of [0, 1]. The updated scheme considers the dilution effects of $O_3$ dose through leaf cross-section by incorporating LMA. Plants with high LMA (e.g., ENF and EBF) usually have low sensitivities, and those with low LMA (e.g., DBF and crops) are more sensitive to $O_3$ damages. The unified sensitivity $a$ is set to 3.5 nmol$^{-1}$ g s and threshold $t$ is set to 0.019 nmol g$^{-1}$ s$^{-1}$ by calibrating simulated $F$ values with literature-based measurements (Ma et al., 2023).

**2.3 Design of simulations**

We perform four sensitivity experiments with the iMAPLE model. The baseline (BASE) simulation considers the two-way coupling between carbon and water cycles, so that the prognostic soil meteorology drives canopy photosynthesis and evapotranspiration. A sensitivity run named BASE_NW is set up by turning off the water cycle in the iMAPLE model. In this simulation, the soil moisture and soil temperature are adopted from the Modern-Era Retrospective Analysis for Research and Applications, Version 2 (MERRA-2) reanalyses (Gelaro et al., 2017). The third and fourth runs turn on the $O_3$ vegetation damage effect using either the LMA-based scheme (O3LMA) or the S2007 scheme (O3S2007). Surface hourly $O_3$ concentrations are adopted from the chemical transport model simulations used in our previous study (Yue and Unger, 2018). For all simulations, the iMAPLE model is driven with the hourly surface meteorology at a spatial resolution of $1º×1º$ from the MERRA-2 reanalyses, including surface air temperature, air pressure, specific humidity, wind speed, precipitation, snowfall, shortwave and longwave radiation. We run the model for the period of 1980-2021 using the initial conditions of the equilibrium soil carbon pool, tree height, and water fluxes from a spin-up run of 200 years driven with perpetual forcing for the year 1980.

The iMAPLE model is driven with observed $CO_2$ concentrations from Mauna Loa (Keeling et al., 1976) and the land cover fraction of nine PFTs derived by combining satellite retrievals from both Moderate Resolution Imaging Spectroradiometer (MODIS) (Hansen et al., 2003) and Advanced Very High Resolution Radiometer (AVHRR) (Defries et al., 2000). For fire emissions, we use Gridded Population of the World version 4 (https://sedac.ciesin.columbia.edu/data/collection/gpw-v4) to calculate human ignition and suppression. The lightning ignition is calculated using the flash rate from Very High Resolution Gridded Lightning Climatology Data CollectionVersion1(https://ghrc.nsstc.nasa.gov/uso/ds_details/collections/lisvhrcC.ht ml). For wetland $CH_4$ emissions, we use the 2000-2020 global dataset of Wetland Area

454 and Dynamics for Methane Modeling (WAD2M) derived from static datasets and

455 remote sensing (Zhang et al., 2021), global soil pH from Hengl et al. (2017), and

456 gridded soil texture from Scholes et al. (2011). For the LMA-based $O_3$ damage scheme,

457 we use gridded LMA from the trait-level dataset of TRY (Kattge et al., 2011) developed

458 by extending field measurements with a random forest model (Moreno-Martínez et al.,

459 2018).

460

461 **2.4 Data for validations**

462 We use observational datasets to validate the biogeochemical processes and related

463 variables simulated by the iMAPLE model. For simulated carbon and water fluxes, site-

464 level observations are collected from 201 sites from the FLUXNET network (Table S2

465 and Figure 2). Among these sites, 95 have the ENF tree species as the major PFT and

466 106 are dominated by non-tree species especially shrubland. Most (71%) of the sites

467 are located at the middle latitudes (30º-60ºN) of the Northern Hemisphere (NH),

468 especially in the U.S. and Europe. Compared to the previous evaluation in YU2015, we

469 have many more sites in the tropics (22 in this study vs. 5 in YU2015), Asia (20 in this

470 study vs. 1 in YU2015), and in the Southern Hemisphere (28 in this study vs. 7 in

471 YU2015) in this study. We also use the global gridded observations of GPP from the

472 satellite retrievals including the solar-induced chlorophyll fluorescence (SIF) product

473 GOSIF (Li and Xiao, 2019) and the Global land surface satellite (GLASS) product

474 (Yuan et al., 2010). The global observations of ET are adopted from the benchmark

475 product of FLUXCOM (Jung et al., 2020a) and the satellite-based GLASS product. For

476 the dynamic fire module, we use monthly observed area burned from the Global Fire

477 Emission Database version 4.1 with small fires (GFED4.1s) during 1997-2016 (van der

478 Werf et al., 2010;Randerson et al., 2012). For methane emissions, we use site-level

479 measurements of $CH_4$ fluxes from the FLUXNET-CH4 network (Delwiche et al., 2021).

480 We exclude the monthly records with missing data at more than half of the days and

481 calculate the long-term mean fluxes for the seasonal cycle. In total, we select 44 sites

482 with at least six months of data available for the validations (Table S3).

483

**3. Model evaluations**

3.1 Site-level evaluations

Simulated GPP shows correlation coefficients (R) of 0.59-0.86 for the six main PFTs with varied sample numbers (Figure 3). The highest R is achieved for ENF, though the model underestimates the mean GPP magnitude by 20.62% for this species. On average, simulated GPP is lower than observations for most PFTs. Compared to previous evaluation of the YIBs model (YU2015), iMAPLE with coupled water cycle improves the R of GPP simulations for ENF (from 0.65 to 0.86) and grassland (from 0.7 to 0.8) but worsens the predictions for other species such as EBF (from 0.65 to 0.59). The main cause of this degradation is the application of MERRA-2 reanalyses in the iMAPLE simulations instead of the site-level meteorology used in the YU2015. The biases in the meteorological input may cause uncertainties in the simulation of GPP fluxes (Ma et al., 2021). In addition, the mismatch of vegetation cover and soil properties between the site location and the 1°×1° grid in the simulation may further contribute to the modeling biases.

499

Simulated ET matches observations with correlation coefficients of 0.57-0.84 at the FLUXNET sites (Figure 4). Relatively better performance is achieved for ENF (R=0.83) and grassland (R=0.84), for which the model yields good predictions of GPP as well. In contrast, low correlations and high biases are predicted for shrubland and cropland. For the shrubland sites, different land types (e.g., closed shrublands, permanent wetlands, and woody savannas) share the same parameters in the iMAPLE model, resulting in the biases in depicting the site-specific carbon and water fluxes. For cropland, the prognostic phenology of grass species is applied in the model due to the missing of plantation information for individual sites. Even with these deficits, the iMAPLE model in general captures the spatiotemporal variations of GPP and ET at most sites.

511

512   We further compare the simulated wetland $CH_4$ fluxes from the BASE experiment with

513   observations at the FLUXNET-$CH_4$ sites. Similar to the carbon flux sites, most of these

514   $CH_4$ flux sites are located in the NH (Figure 5a). However, different from the carbon

515   fluxes which usually range from 0 to 15 g C m$^{-2}$ day$^{-1}$, the $CH_4$ fluxes show a wide

516   range across several orders of magnitude from $10^{-2}$ to $10^3$ g [$CH_4$] m$^{-2}$ yr$^{-1}$ (Figure 5b).

517   Such a large contrast requires a more realistic configuration of model parameters to

518   distinguish the large gradient among sites. For example, US-Tw1 and US-Tw4 are two

519   nearby sites within a distance of 1 km, where our simulations give a $CH_4$ flux of 14.35

520   g[$CH_4$] m$^{-2}$ yr$^{-1}$ during 2011-2017. However, average $CH_4$ flux shows a difference of

521   3.7 times with 66.31 g[$CH_4$] m$^{-2}$ yr$^{-1}$ in US-Tw1 and 18.16 g[$CH_4$] m$^{-2}$ yr$^{-1}$ in US-Tw4

522   during 2011-2017. In the model, these two sites share the same land surface properties

523   because they are located on the same grid. On average, simulated $CH_4$ fluxes are

524   correlated with observations at a moderate R of 0.68 and a normalized mean bias (NMB)

525   of -28%.

526

527   3.2 Grid-level evaluations

528   The coupling of Noah-MP module enables the dynamic prediction of soil parameters

529   by the iMAPLE model. We compare the simulated soil moisture and soil temperature

530   from the BASE experiment with MERRA-2 reanalyses (Figure 6). Both simulations

531   (Figure 6a) and observations (Figure 6b) show low soil moisture over arid and semi-

532   arid regions with the minimum in North Africa. The model also captures the high soil

533   moisture in tropical rainforest. However, the prediction underestimates soil moisture in

534   boreal regions in NH (Figure 6c). On the global scale, simulated soil moisture matches

535   observations with a high R of 0.86 and a low NMB of -6.9%. These statistical metrics

536   are further improved for the simulated soil temperature with the R of 0.99 and NMB of

537   0.5% against observations (Figure 6f). The simulation reproduces the observed spatial

538   pattern with a uniform warming bias.

539

540   Driven with the prognostic soil moisture and temperature, the iMAPLE model predicts

reasonable land carbon and water fluxes (Figure 7). Simulated GPP (Figure 7a) reproduces observed patterns (Figure 7b) with high values in the tropical rainforest, moderate values in the boreal forests, and low values in the arid regions. On the global scale, our simulations yield a total GPP of 129.8 Pg C yr$^{-1}$, similar to the observed amount of 125.4 Pg C yr$^{-1}$. The predicted GPP is higher than observations over the tropical rainforest (Figure 7c). However, such overestimation may instead be an indicator of biases in the ensemble observations, which are derived from the empirical models instead of direct measurements (Yuan et al., 2010;Running et al., 2004). Our site-level evaluations show that iMAPLE predicts reasonable GPP values at the EBF sites (Figure 3). Despite this inconsistency, the model yields a high R of 0.92 and a small NMB of 1.3% for GPP against observations on the global scale (Figure 7c). Simulated ET (Figure 7d) matches the observations (Figure 7e) with high values in the tropical rainforest and secondary high values in the boreal forest. In general, the prediction is lower than observations except for the eastern U.S. and eastern China (Figure 7f). On average, the iMAPLE model shows the R of 0.93 and NMB of -10.4% in the simulation of ET compared to the ensemble of observations.

We further compare the simulated GPP with (BASE) or without (BASE_NW) dynamic water cycle (Figure 8). Relative to the simulations driven with MERRA-2 soil moisture and temperature, the iMAPLE model coupled with Noah-MP water module predicts very similar GPP over the hotspot regions such as tropical rainforest and boreal forest (Figure 8a). However, the coupled model predicts lower GPP for grassland in the tropics (e.g., South America and central Africa) but higher GPP in arid regions (e.g., South Africa and Australia). Since the baseline GPP is very low in arid regions, the relative changes are even larger than 100% over those areas. These GPP differences are mainly driven by the changes in soil moisture, which increases over the arid regions with the dynamic water cycle (Figure 6c). The reduction of soil moisture in the high latitudes of NH shows limited impacts on the predicted GPP, likely because the boreal ecosystem is more dependent on temperature than moisture (Beer et al., 2010).

570

571 3.3 Ecosystem perturbations to air pollution

572 Within the iMAPLE framework, the land ecosystem perturbs atmospheric components

573 through the emissions from biomass burning, wetland $CH_4$, and BVOCs. We compare

574 the simulated burned fraction and fire-emitted organic carbon (OC) emissions with

575 observations from GFED4.1s (Figure 9). The largest burned fraction is predicted over

576 the Sahel region and countries of Angola and Zambia, surrounding the low center of

577 Congo rainforest. Moderate burnings could be found in northern Australia and eastern

578 South America. Most of these hotspots are located on the grassland and shrubland in

579 the tropics, where the high temperature and limited rainfall promotes regional fire

580 activities. The model reasonably captures the observed fire pattern with a spatial

581 correlation of 0.66 and NMB of 6.05% (Figure 9c), though the model overestimates the

582 area burned in South Africa. The predicted fire area is used to derive biomass burning

583 emissions of air pollutants (e.g., carbon monoxide, nitrogen oxides, black carbon,

584 organic carbon, sulfur dioxide) with the specific emission factors (Tian et al., 2023).

585 Furthermore, we compare fire-emitted OC from the model with GFED4.1s. The spatial

586 pattern of OC emissions is similar to that of burned area. The simulations yield a total

587 of 16.8 Tg yr$^{-1}$ for the global fire-emitted OC, slightly higher than the amount of 16.4

588 Tg yr$^{-1}$ from GFED4.1s with some overestimations in tropical Africa (Figure 9f).

589

590 The wetland emissions of $CH_4$ show hotspots over tropical rainforests (Figure 10a),

591 where the dense soil carbon provides abundant substrates for emissions and the warm

592 climate promotes the emission rates. The secondary hotspots are located at the boreal

593 regions in the NH. This spatial pattern is very similar to the map of wetland $CH_4$

594 emissions predicted by an ensemble of 13 biogeochemical models (Saunois et al., 2020).

595 On the global scale, the total wetland emission is 153.45 Tg [$CH_4$] yr$^{-1}$ during 2000-

596 2014, close to the average of 148±25 Tg [$CH_4$] yr$^{-1}$ for 2000-2017 estimated by the

597 multiple models. As a comparison, anthropogenic source of $CH_4$ show the high amount

598 in China and India due to the large emissions from fossil fuels and agriculture (Figure

10b). On the global scale, the wetland emissions are equivalent to 45.3% of the total anthropogenic emissions. As important factors driving $CH_4$ emissions, heterotrophic respiration shows higher values over tropical regions and eastern China with a total amount of 73.2 Pg C yr$^{-1}$ (Figure 10c), and relative high wetland coverages are found in boreal Asia and Amazon (Figure 10d).

Isoprene emissions from the two schemes in the iMAPLE model show similar spatial distributions with the hotspots over tropical rainforest (Figure 11), where the warm climate and abundant light are favorable for the biogenic emissions. Compared to the MEGAN scheme, the PS_BVOC scheme yields higher emissions in the tropical rainforest and boreal forest, but lower emissions for the shrubland and grassland in semiarid regions (Figure 11c). Such differences are attributed to the varied processes as well as the emission factors. Our earlier study showed that PS_BVOC scheme predicts stronger trends in isoprene emissions than MEGAN (Cao et al., 2021a), because the former considers both $CO_2$ fertilization and inhibition effects while the latter considers only the inhibition effects. On the global scale, isoprene emissions are 550 Tg yr$^{-1}$ with PS_BVOC (Figure 11a) and 611 Tg yr$^{-1}$ with MEGAN (Figure 11b). These amounts are higher than the ensemble mean of 448 Tg yr$^{-1}$ from the CMIP6 models (Cao et al., 2021b), but in general within the range of 412-601 Tg yr$^{-1}$ as summarized by Carslaw et al. (2010).

3.4. Air pollution impacts on ecosystem fluxes
We assess the damaging effects of surface $O_3$ to GPP with two schemes (O3LMA – BASE and O3S2007 - BASE) (Figure 12). Simulated GPP losses show similar patterns with high damages in eastern U.S., western Europe, and eastern China, where surface $O_3$ level is high due to the anthropogenic emissions. Limited GPP damages are predicted in the tropics though with abundant forest coverage due to the low level of $O_3$ pollution. Compared to the S2007 scheme, predicted GPP loss is further alleviated in tropical rainforest with the LMA-based scheme, because the latter scheme

628    determines lower $O_3$ sensitivity for evergreen trees due to their higher content of

629    chemical resistance with the larger LMA value (Ma et al., 2023). On the global scale,

630    the average GPP loss is -2.9% with the LMA scheme and -3.2% with the S2007 scheme.

631    Such damage to GPP is weaker than the estimate of -4.8% in Ma et al. (2023) because

632    of the differences in $O_3$ concentrations, vegetation types, and photosynthetic parameters.

633

634    Atmospheric aerosols cause perturbations to both direct and diffuse radiation, which

635    have different efficiencies in enhancing plant photosynthesis. Here, we separate the

636    diffuse (diffuse fraction > 0.75) and direct (diffuse fraction < 0.25) components using

637    observed diffuse fraction and solar radiation at six FLUXNET sites, and aggregate the

638    GPP and ET fluxes for different radiation periods at certain intervals (Figure 13). At the

639    six selected sites, observed GPP is higher and grows faster with more diffusive light

640    than that under the direct light conditions (Figure 13a-13f). Simulations in general

641    reproduce such feature with the comparable variability. In the earlier study, simulated

642    diffuse fertilization efficiency for GPP (changes of GPP per unit diffuse radiation) was

643    well validated against observations at more than 20 sites (Yue and Unger, 2018). Such

644    amelioration of GPP suggests that moderate aerosol loading is beneficial for ecosystem

645    carbon uptake (Yue and Unger, 2017). However, the dense aerosol loading may instead

646    weaken plant photosynthesis due to the large reduction in direct radiation.

647

648    We further evaluate the ET responses to diffuse and direct radiation from the iMAPLE

649    model (Figure 13g-13l). Although ET is slightly higher at the diffusive condition, the

650    growth rates are weaker than that of GPP. The main cause of such difference is related

651    to the varied light dependence of ET components, which consist of canopy evaporation

652    and transpiration. Transpiration is tightly coupled with photosynthesis and will increase

653    by diffuse radiation at a similar rate. However, evaporation is more dependent on light

654    quantity which will decrease with the extinction of aerosols. As a result, the weakened

655    evaporation in part offsets the increased transpiration, leading to the smaller growth rate

656    of ET than the responses of photosynthesis and the consequent enhancement in water

657 use efficiency (Wang et al., 2023). The iMAPLE model reasonably captures the lower

658 growth rates of ET than GPP in response to diffuse radiation at the selected sites.

659

660 **4. Conclusions and discussion**

661 We develop the iMAPLE model by coupling Noah-MP water module with YIBs

662 vegetation model. Validations show that iMAPLE predicts reasonable distribution of

663 soil moisture and soil temperature. Driven with these prognostic soil conditions and

664 meteorology from reanalyses, the model reasonably reproduces the observed

665 spatiotemporal variations of both GPP and ET fluxes at 201 sites and on the global scale.

666 We further update the biogeochemical processes in iMAPLE to extend the model's

667 capability in quantifying interactions between air pollution and land ecosystems. The

668 model reasonably predicts wetland $CH_4$ emissions at 44 sites and yields the similar

669 global map of $CH_4$ emissions compared to an ensemble of 13 biogeochemical models.

670 In addition, predicted biomass burning and biogenic emissions are consistent with

671 either satellite retrievals or results from other models. We assess the impacts of surface

672 $O_3$ and aerosols on ecosystem fluxes. The LMA-based scheme links the $O_3$ sensitivity

673 with vegetation LMA and predicts a global map of GPP loss that is consistent with the

674 traditional scheme using the PFT-specific sensitivity. The updated scheme effectively

675 reduces modeling uncertainties by decreasing the number of parameters for $O_3$

676 sensitivity and provides an option to apply the advanced LMA map from remote sensing.

677 The model also reproduces the observed responses of GPP and ET to diffuse radiation

678 with a lower growth rate for ET than GPP.

679

680 There are several limitations in the current version of iMAPLE. First, it does not include

681 the dynamic nutrient cycle. Although we implement the down regulation from Arora et

682 al. (2009) to constrain $CO_2$ fertilization, this limitation is dependent only on the ambient

683 $CO_2$ concentrations and could not represent the heterogeneous distribution of nutrients.

684 As a result, the model could not reveal the biogeochemical effects of nitrogen and

685 phosphorus deposition on land ecosystems. Second, the feedback of fire activities to

ecosystems is ignored. The iMAPLE model considers the impacts of fuel load on area burned at each modeling time step. However, these fire perturbations do not in turn change the vegetation distribution and composition. The vegetation model does not consider the competition among PFTs, so that fire perturbations are not allowed to change vegetation coverage. As a result, the interactions between fire and ecosystems are underestimated in the current model framework, potentially leading to overestimations of wildfire activity due to remaining fuel loads." Third, iMAPLE does not consider the dynamic changes in wetland area for $CH_4$ emissions. Although the Noah-MP module predicts runoff and underground water, the changes of hydrological cycles are not connected with wetland aera in the model. Instead, a prescribed wetland dataset is applied to reduce the possible uncertainties but meanwhile limits the explorations of $CH_4$ changes in the historical and future periods. Meanwhile, the iMAPLE model considers only dynamic soil water and temperature down to the 2-m level, which may affect the interactions between climate and the land terrestrial ecosystem especially during drier conditions. These limitations will be the focuses of model development in the next step.

The iMAPLE model inherits the good capability of the original YIBs model in the simulations of carbon cycle. Furthermore, iMAPLE upgrades the YIBs model with carbon-water coupling and more biogeochemical processes. With the iMAPLE model, we could assess the changes of carbon and water fluxes, as well as their coupling, in response to environmental perturbations (e.g., climate change, air pollution, land cover change). Meanwhile, by coupling iMAPLE with climate and/or chemical models, we could further quantify the changes of meteorology and atmospheric components in response to the biogeochemical and biogeophysical processes. For example, Lei et al. (2022) revealed the strong vegetation feedback to global surface $O_3$ during the drought periods using the YIBs model coupled to a chemical transport model. Xie et al. (2019) found a significant increase in atmospheric $CO_2$ concentrations due to $O_3$-induced vegetation damage using the YIBs model coupled with a regional climate-chemistry

model. Gong et al. (2021) estimated a surface warming in polluted regions due to the ozone-vegetation feedback using the YIBs model coupled with a global climate-chemistry model. These studies indicate that the iMAPLE model could be used either offline or online with other models to explore the interactions among climate, chemistry, and ecosystems.

*Acknowledgment*. This work was jointly supported by the National Key Research and Development Program of China (grant no. 2019YFA0606802), the National Natural Science Foundation of China (grant no. 42275128), and the Natural Science Foundation of Jiangsu Province (grant no. BK20220031).

*Author contributions*. XY designed the research and wrote the paper. XY, HaZ optimized codes, performed simulations, and analyzed results. HaZ, CT, YM, YH, CG implemented codes and collected data. HuZ helped with code implementations. All authors commented on and revised the manuscript.

*Competing interests*. The contact author has declared that none of the authors has any competing interests.

*Code availability*. The code for the iMAPLE version 1 model is available at https://doi.org/10.6084/m9.figshare.23593578.v1

*Data availability*. All the validation data are available to download from the cited references or data links shown in Section 2.4. The simulation data of monthly output from the BASE experiment during 1980-2021 with the iMAPLE model are available at https://doi.org/10.6084/m9.figshare.23593578.v1

**Reference**

Arora, V. K., Boer, G. J., Christian, J. R., Curry, C. L., Denman, K. L., Zahariev, K., Flato, G. M., Scinocca, J. F., Merryfield, W. J., and Lee, W. G.: The Effect of

Terrestrial Photosynthesis Down Regulation on the Twentieth-Century Carbon Budget Simulated with the CCCma Earth System Model, J Climate, 22, 6066-6088, 10.1175/2009jcli3037.1, 2009.

Ball, J. T., Woodrow, I. E., and Berry, J. A.: A model predicting stomatal conductance and its contribution to the control of photosyn- thesis under different environmental conditions, in: Progress in Photosynthesis Research, edited by: Biggins, J., Nijhoff, Dordrecht, Netherlands, 221-224, 1987.

Beer, C., Reichstein, M., Tomelleri, E., Ciais, P., Jung, M., Carvalhais, N., Rodenbeck, C., Arain, M. A., Baldocchi, D., Bonan, G. B., Bondeau, A., Cescatti, A., Lasslop, G., Lindroth, A., Lomas, M., Luyssaert, S., Margolis, H., Oleson, K. W., Roupsard, O., Veenendaal, E., Viovy, N., Williams, C., Woodward, F. I., and Papale, D.: Terrestrial Gross Carbon Dioxide Uptake: Global Distribution and Covariation with Climate, Science, 329, 834-838, 10.1126/Science.1184984, 2010.

Cao, Y., Yue, X., Lei, Y., Zhou, H., Liao, H., Song, Y., Bai, J., Yang, Y., Chen, L., Zhu, J., Ma, Y., and Tian, C.: Identifying the drivers of modeling uncertainties in isoprene emissions: schemes versus meteorological forcings, Journal of Geophysical Research, 126, e2020JD034242, 10.1029/2020JD034242, 2021a.

Cao, Y., Yue, X., Liao, H., Yang, Y., Zhu, J., Chen, L., Tian, C., Lei, Y., Zhou, H., and Ma, Y.: Ensemble projection of global isoprene emissions by the end of 21$^{st}$ century using CMIP6 models, Atmospheric Environment, 267, 118766, 10.1016/j.atmosenv.2021.118766, 2021b.

Carslaw, K. S., Boucher, O., Spracklen, D. V., Mann, G. W., Rae, J. G. L., Woodward, S., and Kulmala, M.: A review of natural aerosol interactions and feedbacks within the Earth system, Atmos Chem Phys, 10, 1701-1737, 10.5194/acp-10-1701-2010, 2010.

Castillo, C. K. G., Levis, S., and Thornton, P.: Evaluation of the New CNDV Option of the Community Land Model: Effects of Dynamic Vegetation and Interactive Nitrogen on CLM4 Means and Variability, J Climate, 25, 3702-3714, 10.1175/Jcli-D-11-00372.1, 2012.

Chen, G., Guo, Y., Yue, X., Tong, S., Gasparrini, A., Bell, M. L., Armstrong, B., Schwartz, J., Jouni J K Jaakkola, Zanobetti, A., Lavigne, E., Saldiva, P. H. N., Kan, H., Royé, D., Milojevic, A., Overcenco, A., Urban, A., Schneider, A., Entezari, A., Vicedo-Cabrera, A. M., Zeka, A., Tobias, A., Nunes, B., Alahmad, B., Bertil Forsberg, Pan, S.-C., Íñiguez, C., Ameling, C., Valencia, C. D. l. C., Åström, C., Houthuijs, D., Dung, D. V., Samoli, E., Mayvaneh, F., Sera, F., Carrasco-Escobar, G., Lei, Y., Orru, H., Kim, H., Iulian-Horia Holobaca, Kyselý, J., Teixeira, J. P., Madureira, J., Katsouyanni, K., Hurtado-Díaz, M., Maasikmets, M., Ragettli, M. S., Hashizume, M., Stafoggia, M., Pascal, M., Scortichini, M., Micheline de Sousa Zanotti Stagliorio Coêlho, Ortega, N. V., Ryti, N. R. I., Scovronick, N., Matus, P., Goodman, P., Garland, R. M., Abrutzky, R., Garcia, S. O., Rao, S., Fratianni, S., Dang, T. N., Colistro, V., Huber, V., Lee, W., Seposo, X., Honda, Y., Guo, Y. L., Ye, T., Yu, W., Abramson, M. J., Samet, J. M., and Li, S.: Mortality risk attributable to wildfire-related PM2·5 pollution: a global time series study in 749 locations, The Lancet Planetary Health, 5, e579-e587, 10.1016/S2542-5196(21)00200-X, 2021.

Clapp, R. B., and Hornberger, G. M.: Empirical equations for some soil hydraulic properties, Water Resources Research, 14, 601-604, 1978.

Cox, P. M.: Description of the "TRIFFID" Dynamic Global Vegetation Model, Hadley Centre technical note 24, Berks, UK, 2001.

Defries, R. S., Hansen, M. C., Townshend, J. R. G., Janetos, A. C., and Loveland, T. R.: A new global 1-km dataset of percentage tree cover derived from remote sensing, Global Change Biology, 6, 247-254, 10.1046/j.1365-2486.2000.00296.x, 2000.

Delwiche, K. B., Knox, S. H., Malhotra, A., Fluet-Chouinard, E., McNicol, G., Feron, S., Ouyang, Z., Papale, D., Trotta, C., Canfora, E., Cheah, Y. W., Christianson, D., Alberto, M. C. R., Alekseychik, P., Aurela, M., Baldocchi, D., Bansal, S., Billesbach, D. P., Bohrer, G., Bracho, R., Buchmann, N., Campbell, D. I., Celis, G., Chen, J., Chen, W., Chu, H., Dalmagro, H. J., Dengel, S., Desai, A. R., Detto, M., Dolman, H., Eichelmann, E., Euskirchen, E., Famulari, D., Fuchs, K., Goeckede, M., Gogo, S., Gondwe, M. J., Goodrich, J. P., Gottschalk, P., Graham, S. L., Heimann, M., Helbig, M., Helfter, C., Hemes, K. S., Hirano, T., Hollinger, D., Hörtnagl, L., Iwata, H., Jacotot, A., Jurasinski, G., Kang, M., Kasak, K., King, J., Klatt, J., Koebsch, F., Krauss, K. W., Lai, D. Y. F., Lohila, A., Mammarella, I., Belelli Marchesini, L., Manca, G., Matthes, J. H., Maximov, T., Merbold, L., Mitra, B., Morin, T. H., Nemitz, E., Nilsson, M. B., Niu, S., Oechel, W. C., Oikawa, P. Y., Ono, K., Peichl, M., Peltola, O., Reba, M. L., Richardson, A. D., Riley, W., Runkle, B. R. K., Ryu, Y., Sachs, T., Sakabe, A., Sanchez, C. R., Schuur, E. A., Schäfer, K. V. R., Sonnentag, O., Sparks, J. P., Stuart-Haëntjens, E., Sturtevant, C., Sullivan, R. C., Szutu, D. J., Thom, J. E., Torn, M. S., Tuittila, E. S., Turner, J., Ueyama, M., Valach, A. C., Vargas, R., Varlagin, A., Vazquez-Lule, A., Verfaillie, J. G., Vesala, T., Vourlitis, G. L., Ward, E. J., Wille, C., Wohlfahrt, G., Wong, G. X., Zhang, Z., Zona, D., Windham-Myers, L., Poulter, B., and Jackson, R. B.: FLUXNET-CH4: a global, multi-ecosystem dataset and analysis of methane seasonality from freshwater wetlands, Earth Syst. Sci. Data, 13, 3607-3689, 10.5194/essd-13-3607-2021, 2021.

Farquhar, G. D., Caemmerer, S. V., and Berry, J. A.: A biochemical-model of photosynthetic $CO_2$ assimilation in leaves of C-3 species, Planta, 149, 78-90, 10.1007/bf00386231, 1980.

Friedlingstein, P., O'Sullivan, M., Jones, M. W., Andrew, R. M., Hauck, J., Olsen, A., Peters, G. P., Peters, W., Pongratz, J., Sitch, S., Quéré, C. L., Canadell, J. G., Ciais, P. P., Jackson, R. B., Alin, S., Aragao, L. E., Arneth, A., Arora, V., Bates, N. R., Becker, M., Benoit-Cattin, A., Bittig, H. C., Bopp, L., Bultan, S., Chandra, N., Chevallier, F., Chini, L. P., Evans, W., Florentie, L., Forster, P. M., Gasser, T., Gehlen, M., Gilfillan, D., Gkritzalis, T., Gregor, L., Gruber, N., Harris, I., Hartung, K., Haverd, V., Houghton, R. A., Ilyina, T., Jain, A. K., Joetzjer, E., Kadono, K., Kato, E., Kitidis, V., Ivar, J. I. J., Landschützer, P., Lefèvre, N., Lenton, A., Lienert, S., Liu, Z., Lombardozzi, D., Marland, G., Metzl, N., Munro, D. R., Nabel, J. E., Nakaoka, S.-I., Niwa, Y., O′Brien, K., Ono, T., Palmer, P. I., Pierrot, D., Poulter, B., Resplandy, L., Robertson, E., Rödenbeck, C., Schwinger, J., Séférian, R., Skjelvan, I., Smith, A. J., Sutton, A., Tanhua, T., Tans, P. P., Tian, H., Tilbrook, B.,

Werf, G. R. v. d., Vuichard, N., Walker, A., Wanninkhof, R., Watson, A. J., Willis, D., Wiltshire, A. J., Yuan, W., Yue, X., and Zaehle, S.: Global Carbon Budget 2020, Earth System Science Data, 12, 3269-3340, 2020.

Friedlingstein, P., O'Sullivan, M., Jones, M. W., Andrew, R. M., Gregor, L., Hauck, J., Quéré, C. L., Luijkx, I. T., Olsen, A., Peters, G. P., Peters, W., Pongratz, J., Schwingshackl, C., Sitch, S., Canadell, J. G., Ciais, P., Jackson, R. B., Alin, S. R., Alkama, R., Arneth, A., Arora, V. K., Bates, N. R., Becker, M., Bellouin, N., Bittig, H. C., Bopp, L., Chevallier, F., Chini, L. P., Cronin, M., Decharme, B., Evans, W., Falk, S., Feely, R. A., Gasser, T., Gehlen, M., Gkritzalis, T., Gloege, L., Grassi, G., Gruber, N., Gürses, Ö., Harris, I., Hefner, M., Houghton, R. A., Hurtt, G. C., Iida, Y., Ilyina, T., Jain, A. K., Jersild, A., Kadono, K., Kato, E., Kennedy, D., Goldewijk, K. K., Knauer, J., Korsbakken, J. I., Landschützer, P., Lefèvre, N., Lindsay, K., Liu, Z., Liu, J., Marland, G., Mayot, N., McGrath, M. J., Metzl, N., Monacci, N. M., Munro, D. R., Nakaoka, S.-I., Niwa, Y., O'Brien, K., Ono, T., Palmer, P. I., Pan, N., Pierrot, D., Pocock, K., Poulter, B., Resplandy, L., Robertson, E., Rödenbeck, C., Rodriguez, C., Rosan, T. M., Schwinger, J., Séférian, R., Shutler, J. D., Skjelvan, I., Steinhoff, T., Sun, Q., Sutton, A. J., Sweeney, C., Takao, S., Tanhua, T., Tans, P. P., Tian, X., Tian, H., Tilbrook, B., Tsujino, H., Tubiello, F., Werf, G. v. d., Walker, A. P., Wanninkhof, R., Whitehead, C., Wranne, A. W., Wright, R., Yuan, W., Yue, C., Yue, X., Zaehle, S., Zeng, J., and Zheng, B.: Global Carbon Budget 2022, Earth System Science Data, 14, 4811-4900, 10.5194/essd-14-4811-2022, 2022.

Gelaro, R., McCarty, W., Suarez, M. J., Todling, R., Molod, A., Takacs, L., Randles, C. A., Darmenov, A., Bosilovich, M. G., Reichle, R., Wargan, K., Coy, L., Cullather, R., Draper, C., Akella, S., Buchard, V., Conaty, A., da Silva, A. M., Gu, W., Kim, G. K., Koster, R., Lucchesi, R., Merkova, D., Nielsen, J. E., Partyka, G., Pawson, S., Putman, W., Rienecker, M., Schubert, S. D., Sienkiewicz, M., and Zhao, B.: The Modern-Era Retrospective Analysis for Research and Applications, Version 2 (MERRA-2), J Climate, 30, 5419-5454, 10.1175/Jcli-D-16-0758.1, 2017.

Gong, C., Liao, H., Yue, X., Ma, Y., and Lei, Y.: Impacts of ozone-vegetation interactions on ozone pollution episodes in North China and the Yangtze River Delta, Geophysical Research Letters, 48, e2021GL093814, 10.1029/2021GL093814, 2021.

Guenther, A. B., Jiang, X., Heald, C. L., Sakulyanontvittaya, T., Duhl, T., Emmons, L. K., and Wang, X.: The Model of Emissions of Gases and Aerosols from Nature version 2.1 (MEGAN2.1): an extended and updated framework for modeling biogenic emissions, Geosci Model Dev, 5, 1471-1492, 10.5194/Gmd-5-1471-2012, 2012.

Hansen, M. C., DeFries, R. S., Townshend, J. R. G., Carroll, M., Dimiceli, C., and Sohlberg, R. A.: Global Percent Tree Cover at a Spatial Resolution of 500 Meters: First Results of the MODIS Vegetation Continuous Fields Algorithm, Earth Interact, 7, 1-15, 10.1175/1087-3562(2003)007<0001:GPTCAA>2.0.CO;2, 2003.

Heimann, I., Griffiths, P. T., Warwick, N. J., Abraham, N. L., Archibald, A. T., and Pyle, J. A.: Methane Emissions in a Chemistry-Climate Model: Feedbacks and Climate Response, J Adv Model Earth Sy, 12, e2019MS002019, 10.1029/2019MS002019,

2020.

Hengl, T., de Jesus, J. M., Heuvelink, G. B. M., Gonzalez, M. R., Kilibarda, M., Blagotic, A., Shangguan, W., Wright, M. N., Geng, X. Y., Bauer-Marschallinger, B., Guevara, M. A., Vargas, R., MacMillan, R. A., Batjes, N. H., Leenaars, J. G. B., Ribeiro, E., Wheeler, I., Mantel, S., and Kempen, B.: SoilGrids250m: Global gridded soil information based on machine learning, Plos One, 12, ARTN e0169748

10.1371/journal.pone.0169748, 2017.

Jasechko, S., Sharp, Z. D., Gibson, J. J., Birks, S. J., Yi, Y., and Fawcett, P. J.: Terrestrial water fluxes dominated by transpiration, Nature, 496, 347-350, 10.1038/nature11983, 2013.

Jung, M., Reichstein, M., Margolis, H. A., Cescatti, A., Richardson, A. D., Arain, M. A., Arneth, A., Bernhofer, C., Bonal, D., Chen, J. Q., Gianelle, D., Gobron, N., Kiely, G., Kutsch, W., Lasslop, G., Law, B. E., Lindroth, A., Merbold, L., Montagnani, L., Moors, E. J., Papale, D., Sottocornola, M., Vaccari, F., and Williams, C.: Global patterns of land-atmosphere fluxes of carbon dioxide, latent heat, and sensible heat derived from eddy covariance, satellite, and meteorological observations, Journal of Geophysical Research, 116, G00j07, 10.1029/2010jg001566, 2011.

Jung, M., Schwalm, C., Migliavacca, M., Walther, S., Camps-Valls, G., Koirala, S., Anthoni, P., Besnard, S., Bodesheim, P., Carvalhais, N., Chevallier, F., Gans, F., Goll, D. S., Haverd, V., Köhler, P., Ichii, K., Jain, A. K., Liu, J., Lombardozzi, D., Nabel, J. E. M. S., Nelson, J. A., O'Sullivan, M., Pallandt, M., Papale, D., Peters, W., Pongratz, J., Rödenbeck, C., Sitch, S., Tramontana, G., Walker, A., Weber, U., and Reichstein, M.: Scaling carbon fluxes from eddy covariance sites to globe: synthesis and evaluation of the FLUXCOM approach, Biogeosciences, 17, 1343-1365, 10.5194/bg-17-1343-2020, 2020a.

Jung, M., Schwalm, C., Migliavacca, M., Walther, S., Camps-Valls, G., Koirala, S., Anthoni, P., Besnard, S., Bodesheim, P., Carvalhais, N., Chevallier, F., Gans, F., Goll, D. S., Haverd, V., Kohler, P., Ichii, K., Jain, A. K., Liu, J. Z., Lombardozzi, D., Nabel, J. E. M. S., Nelson, J. A., O'Sullivan, M., Pallandt, M., Papale, D., Peters, W., Pongratz, J., Rodenbeck, C., Sitch, S., Tramontana, G., Walker, A., Weber, U., and Reichstein, M.: Scaling carbon fluxes from eddy covariance sites to globe: synthesis and evaluation of the FLUXCOM approach, Biogeosciences, 17, 1343-1365, 10.5194/bg-17-1343-2020, 2020b.

Kattge, J., Diaz, S., Lavorel, S., Prentice, C., Leadley, P., Bonisch, G., Garnier, E., Westoby, M., Reich, P. B., Wright, I. J., Cornelissen, J. H. C., Violle, C., Harrison, S. P., van Bodegom, P. M., Reichstein, M., Enquist, B. J., Soudzilovskaia, N. A., Ackerly, D. D., Anand, M., Atkin, O., Bahn, M., Baker, T. R., Baldocchi, D., Bekker, R., Blanco, C. C., Blonder, B., Bond, W. J., Bradstock, R., Bunker, D. E., Casanoves, F., Cavender-Bares, J., Chambers, J. Q., Chapin, F. S., Chave, J., Coomes, D., Cornwell, W. K., Craine, J. M., Dobrin, B. H., Duarte, L., Durka, W., Elser, J., Esser, G., Estiarte, M., Fagan, W. F., Fang, J., Fernandez-Mendez, F., Fidelis, A., Finegan, B., Flores, O., Ford, H., Frank, D., Freschet, G. T., Fyllas, N.

M., Gallagher, R. V., Green, W. A., Gutierrez, A. G., Hickler, T., Higgins, S. I., Hodgson, J. G., Jalili, A., Jansen, S., Joly, C. A., Kerkhoff, A. J., Kirkup, D., Kitajima, K., Kleyer, M., Klotz, S., Knops, J. M. H., Kramer, K., Kuhn, I., Kurokawa, H., Laughlin, D., Lee, T. D., Leishman, M., Lens, F., Lenz, T., Lewis, S. L., Lloyd, J., Llusia, J., Louault, F., Ma, S., Mahecha, M. D., Manning, P., Massad, T., Medlyn, B. E., Messier, J., Moles, A. T., Muller, S. C., Nadrowski, K., Naeem, S., Niinemets, U., Nollert, S., Nuske, A., Ogaya, R., Oleksyn, J., Onipchenko, V. G., Onoda, Y., Ordonez, J., Overbeck, G., Ozinga, W. A., Patino, S., Paula, S., Pausas, J. G., Penuelas, J., Phillips, O. L., Pillar, V., Poorter, H., Poorter, L., Poschlod, P., Prinzing, A., Proulx, R., Rammig, A., Reinsch, S., Reu, B., Sack, L., Salgado-Negre, B., Sardans, J., Shiodera, S., Shipley, B., Siefert, A., Sosinski, E., Soussana, J. F., Swaine, E., Swenson, N., Thompson, K., Thornton, P., Waldram, M., Weiher, E., White, M., White, S., Wright, S. J., Yguel, B., Zaehle, S., Zanne, A. E., and Wirth, C.: TRY - a global database of plant traits, Global Change Biology, 17, 2905-2935, 10.1111/j.1365-2486.2011.02451.x, 2011.

Keeling, C. D., Bacastow, R. B., Bainbridge, A. E., Ekdahl, C. A., Guenther, P. R., Waterman, L. S., and Chin, J. F. S.: Atmospheric carbon dioxide variations at Mauna Loa Observatory, Hawaii, Tellus A., 28, 538-551, 10.1111/j.2153-3490.1976.tb00701.x, 1976.

Lei, Y., Yue, X., Liao, H., Gong, C., and Zhang, L.: Implementation of Yale Interactive terrestrial Biosphere model v1.0 into GEOS-Chem v12.0.0: a tool for biosphere-chemistry interactions, Geosci Model Dev, 13, 1137-1153, 10.5194/gmd-13-1137-2020, 2020.

Lei, Y., Yue, X., Liao, H., Zhang, L., Zhou, H., Tian, C., Gong, C., Ma, Y., Cao, Y., Seco, R., Karl, T., and Potosnak, M.: Global perspective of drought impacts on ozone pollution episodes, Environmental Science & Technology, 56, 3932-3940, 2022.

Li, F., Zeng, X. D., and Levis, S.: A process-based fire parameterization of intermediate complexity in a Dynamic Global Vegetation Model (vol 9, pg 2761, 2012), Biogeosciences, 9, 4771-4772, 10.5194/bg-9-4771-2012, 2012.

Li, X., and Xiao, J.: Mapping Photosynthesis Solely from Solar-Induced Chlorophyll Fluorescence: A Global, Fine-Resolution Dataset of Gross Primary Production Derived from OCO-2, Remote Sensing, 11, 2563, 10.3390/rs11212563, 2019.

Lin, M. Y., Horowitz, L. W., Xie, Y. Y., Paulot, F., Malyshev, S., Shevliakova, E., Finco, A., Gerosa, G., Kubistin, D., and Pilegaard, K.: Vegetation feedbacks during drought exacerbate ozone air pollution extremes in Europe, Nat Clim Change, 10, 444-451, 10.1038/s41558-020-0743-y, 2020.

Lombardozzi, D., Levis, S., Bonan, G., Hess, P. G., and Sparks, J. P.: The Influence of Chronic Ozone Exposure on Global Carbon and Water Cycles, J Climate, 28, 292-305, 10.1175/Jcli-D-14-00223.1, 2015.

Ma, Y., Yue, X., Zhou, H., Gong, C., Lei, Y., Tian, C., and Cao, Y.: Identifying the dominant climate-driven uncertainties in modeling gross primary productivity, Science of the Total Environment, 800, 149518, 10.1016/j.scitotenv.2021.149518, 2021.

Ma, Y., Yue, X., Sitch, S., Unger, N., Uddling, J., Mercado, L. M., Gong, C., Feng, Z.,

Yang, H., Zhou, H., Tian, C., Cao, Y., Lei, Y., Cheesman, A. W., Xu, Y., and Rojas, M. C. D.: Implementation of trait-based ozone plant sensitivity in the Yale Interactive terrestrial Biosphere model v1.0 to assess global vegetation damage, Geosci Model Dev, 16, 2261-2276, 10.5194/gmd-16-2261-2023, 2023.

Madani, N., Kimball, J. S., and Running, S. W.: Improving Global Gross Primary Productivity Estimates by Computing Optimum Light Use Efficiencies Using Flux Tower Data, Journal of Geophysical Research-Biogeosciences, 122, 2939-2951, 10.1002/2017jg004142, 2017.

Mercado, L. M., Bellouin, N., Sitch, S., Boucher, O., Huntingford, C., Wild, M., and Cox, P. M.: Impact of changes in diffuse radiation on the global land carbon sink, Nature, 458, 1014-U1087, 10.1038/Nature07949, 2009.

Moreno-Martínez, Á., Camps-Valls, G., Kattge, J., Robinson, N., Reichstein, M., Bodegom, P. V., and Running, S. W.: Global maps of leaf traits at 3km resolution, TRY File Archive, in, 2018.

Niu, G. Y., Yang, Z. L., Mitchell, K. E., Chen, F., Ek, M. B., Barlage, M., Kumar, A., Manning, K., Niyogi, D., Rosero, E., Tewari, M., and Xia, Y. L.: The community Noah land surface model with multiparameterization options (Noah-MP): 1. Model description and evaluation with local-scale measurements, Journal of Geophysical Research, 116, D12109, 10.1029/2010jd015139, 2011.

Paudel, R., Mahowald, N. M., Hess, P. G. M., Meng, L., and Riley, W. J.: Attribution of changes in global wetland methane emissions from pre-industrial to present using CLM4.5-BGC, Environ Res Lett, 11, 034020, 10.1088/1748-9326/11/3/034020, 2016.

Pechony, O., and Shindell, D. T.: Fire parameterization on a global scale, Journal of Geophysical Research-Atmospheres, 114, D16115, 10.1029/2009jd011927, 2009.

Piao, S. L., Ciais, P., Friedlingstein, P., de Noblet-Ducoudre, N., Cadule, P., Viovy, N., and Wang, T.: Spatiotemporal patterns of terrestrial carbon cycle during the 20th century, Global Biogeochem Cy, 23, Gb4026, 10.1029/2008gb003339, 2009.

Randerson, J. T., Chen, Y., van der Werf, G. R., Rogers, B. M., and Morton, D. C.: Global burned area and biomass burning emissions from small fires, Journal of Geophysical Research-Biogeosciences, 117, G04012, 10.1029/2012jg002128, 2012.

Rap, A., Scott, C. E., Reddington, C. L., Mercado, L., Ellis, R. J., Garraway, S., Evans, M. J., Beerling, D. J., MacKenzie, A. R., Hewitt, C. N., and Spracklen, D. V.: Enhanced global primary production by biogenic aerosol via diffuse radiation fertilization, Nat Geosci, 11, 640-644, 10.1038/s41561-018-0208-3, 2018.

Rosentreter, J. A., Borges, A. V., Deemer, B. R., Holgerson, M. A., Liu, S. D., Song, C. L., Melack, J., Raymond, P. A., Duarte, C. M., Allen, G. H., Olefeldt, D., Poulter, B., Battin, T. I., and Eyre, B. D.: Half of global methane emissions come from highly variable aquatic ecosystem sources, Nature Geoscience, 14, 225-+, 10.1038/s41561-021-00715-2, 2021.

Running, S., Nemani, R., Heinsch, F., Zhao, M., Reeves, M., and Hashimoto, H.: A continuous satellite-derived measure of global terrestrial primary production, BioScience, 54, 547-560, 10.1641/0006-

3568(2004)054[0547:ACSMOG]2.0.CO;2, 2004.

Saunois, M., Stavert, A. R., Poulter, B., Bousquet, P., Canadell, J. G., Jackson, R. B., Raymond, P. A., Dlugokencky, E. J., Houweling, S., Patra, P. K., Ciais, P., Arora, V. K., Bastviken, D., Bergamaschi, P., Blake, D. R., Brailsford, G., Bruhwiler, L., Carlson, K. M., Carrol, M., Castaldi, S., Chandra, N., Crevoisier, C., Crill, P. M., Covey, K., Curry, C. L., Etiope, G., Frankenberg, C., Gedney, N., Hegglin, M. I., Hoglund-Isaksson, L., Hugelius, G., Ishizawa, M., Ito, A., Janssens-Maenhout, G., Jensen, K. M., Joos, F., Kleinen, T., Krummel, P. B., Langenfelds, R. L., Laruelle, G. G., Liu, L. C., Machida, T., Maksyutov, S., McDonald, K. C., McNorton, J., Miller, P. A., Melton, J. R., Morino, I., Muller, J., Murguia-Flores, F., Naik, V., Niwa, Y., Noce, S., Doherty, S. O., Parker, R. J., Peng, C. H., Peng, S. S., Peters, G. P., Prigent, C., Prinn, R., Ramonet, M., Regnier, P., Riley, W. J., Rosentreter, J. A., Segers, A., Simpson, I. J., Shi, H., Smith, S. J., Steele, L. P., Thornton, B. F., Tian, H. Q., Tohjima, Y., Tubiello, F. N., Tsuruta, A., Viovy, N., Voulgarakis, A., Weber, T. S., van Weele, M., van der Werf, G. R., Weiss, R. F., Worthy, D., Wunch, D., Yin, Y., Yoshida, Y., Zhang, W. X., Zhang, Z., Zhao, Y. H., Zheng, B., Zhu, Q., Zhu, Q. A., and Zhuang, Q. L.: The Global Methane Budget 2000-2017, Earth System Science Data, 12, 1561-1623, 10.5194/essd-12-1561-2020, 2020.

Schaake, J. C., Koren, V. I., Duan, Q.-Y., Mitchell, K., and Chen, F.: Simple water balance model for estimating runoff at different spatial and temporal scales, Journal of Geophysical Research, 101, 7461-7475, 10.1029/95JD02892, 1996.

Schaefer, K., Collatz, G. J., Tans, P., Denning, A. S., Baker, I., Berry, J., Prihodko, L., Suits, N., and Philpott, A.: Combined Simple Biosphere/Carnegie-Ames-Stanford Approach terrestrial carbon cycle model, J Geophys Res-Biogeo, 113, G03034, 10.1029/2007jg000603, 2008.

Scholes, R. J., Colstoun, E. B. d., Hall, F. G., Collatz, G. J., Meeson, B. W., Los, S. O., and Landis, D. R.: ISLSCP II Global Gridded Soil Characteristics, in, ORNL DAAC, Oak Ridge, Tennessee, USA, 2011.

Sitch, S., Cox, P. M., Collins, W. J., and Huntingford, C.: Indirect radiative forcing of climate change through ozone effects on the land-carbon sink, Nature, 448, 791-U794, 10.1038/nature06059, 2007.

Sitch, S., Friedlingstein, P., Gruber, N., Jones, S. D., Murray-Tortarolo, G., Ahlström, A., Doney, S. C., Graven, H., Heinze, C., Huntingford, C., Levis, S., Levy, P. E., Lomas, M., Poulter, B., Viovy, N., Zaehle, S., Zeng, N., Arneth, A., Bonan, G., Bopp, L., Canadell, J. G., Chevallier, F., Ciais, P., Ellis, R., Gloor, M., Peylin, P., Piao, S. L., Quéré, C. L., Smith, B., Zhu, Z., and Myneni, R.: Recent trends and drivers of regional sources and sinks of carbon dioxide, Biogeosciences, 12, 653-679, 2015.

Spitters, C. J. T.: Separating the Diffuse and Direct Component of Global Radiation and Its Implications for Modeling Canopy Photosynthesis .2. Calculation of Canopy Photosynthesis, Agr Forest Meteorol, 38, 231-242, 10.1016/0168-1923(86)90061-4, 1986.

Spracklen, D. V., Arnold, S. R., and Taylor, C. M.: Observations of increased tropical rainfall preceded by air passage over forests, Nature, 489, 282-U127, 2012.

Terrer, C., Jackson, R. B., Prentice, I. C., Keenan, T. F., Kaiser, C., Vicca, S., Fisher, J. B., Reich, P. B., Stocker, B. D., Hungate, B. A., Penuelas, J., McCallum, I., Soudzilovskaia, N. A., Cernusak, L. A., Talhelm, A. F., Van Sundert, K., Piao, S. L., Newton, P. C. D., Hovenden, M. J., Blumenthal, D. M., Liu, Y. Y., Muller, C., Winter, K., Field, C. B., Viechtbauer, W., Van Lissa, C. J., Hoosbeek, M. R., Watanabe, M., Koike, T., Leshyk, V. O., Polley, H. W., and Franklin, O.: Nitrogen and phosphorus constrain the CO2 fertilization of global plant biomass, Nat Clim Change, 9, 684-689, 10.1038/s41558-019-0545-2, 2019.

Tian, C., Yue, X., Zhu, J., Liao, H., Yang, Y., Lei, Y., Zhou, X., Zhou, H., Ma, Y., and Cao, Y.: Fire-climate interactions through aerosol radiative effect in a global chemistry-climate-vegetation model, Atmospheric Chemistry and Physics, 22, 12353-12366, 10.5194/acp-22-12353-2022, 2022.

Tian, C., Yue, X., Zhu, J., Liao, H., Yang, Y., Chen, L., Zhou, X., Lei, Y., Zhou, H., and Cao, Y.: Projections of fire emissions and the consequent impacts on air quality under 1.5°C and 2°C global warming, Environ Pollut, 323, 121311, 10.1016/j.envpol.2023.121311, 2023.

Unger, N., Harper, K., Zheng, Y., Kiang, N. Y., Aleinov, I., Arneth, A., Schurgers, G., Amelynck, C., Goldstein, A., Guenther, A., Heinesch, B., Hewitt, C. N., Karl, T., Laffineur, Q., Langford, B., McKinney, K. A., Misztal, P., Potosnak, M., Rinne, J., Pressley, S., Schoon, N., and Serça, D.: Photosynthesis-dependent isoprene emission from leaf to planet in a global carbon–chemistry–climate model, Atmos. Chem. Phys., 13, 10243-10269, 10.5194/acp-13-10243-2013, 2013.

van der Werf, G. R., Randerson, J. T., Giglio, L., Collatz, G. J., Mu, M., Kasibhatla, P. S., Morton, D. C., DeFries, R. S., Jin, Y., and van Leeuwen, T. T.: Global fire emissions and the contribution of deforestation, savanna, forest, agricultural, and peat fires (1997-2009), Atmos Chem Phys, 10, 11707-11735, 10.5194/Acp-10-11707-2010, 2010.

Walter, B. P., and Heimann, M.: A process-based, climate-sensitive model to derive methane emissions from natural wetlands: Application to five wetland sites, sensitivity to model parameters, and climate, Global Biogeochem Cy, 14, 745-765, 10.1029/1999GB001204, 2000.

Walter, B. P., Heimann, M., and Matthews, E.: Modeling modern methane emissions from natural wetlands: 1. Model description and results, Journal of Geophysical Research, 106, 34189-34206, 10.1029/2001JD900165, 2001.

Wang, B., Yue, X., Zhou, H., Lu, X., and Zhu, J.: Enhanced ecosystem water-use efficiency under the more diffuse radiation conditions, Global Biogeochemical Cycles, 37, e2022GB007606, 10.1029/2022GB007606, 2023.

Wang, S. H., Zhang, Y. G., Ju, W. M., Chen, J. M., Ciais, P., Cescatti, A., Sardans, J., Janssens, I. A., Wu, M. S., Berry, J. A., Campbell, E., Fernandez-Martinez, M., Alkama, R., Sftch, S., Friedlingstein, P., Smith, W. K., Yuan, W. P., He, W., Lombardozzi, D., Kautz, M., Zhu, D., Lienert, S., Kato, E., Poulter, B., Sanders, T. G. M., Kruger, I., Wang, R., Zeng, N., Tian, H. Q., Vuichard, N., Jain, A. K., Wiltshire, A., Haverd, V., Goll, D. S., and Penuelas, J.: Recent global decline of CO2 fertilization effects on vegetation photosynthesis, Science, 370, 1295-1300,

10.1126/science.abb7772, 2020.

Wania, R., Ross, I., and Prentice, I. C.: Implementation and evaluation of a new methane model within a dynamic global vegetation model: LPJ-WHyMe v1.3.1, Geosci Model Dev, 3, 565-584, 10.5194/gmd-3-565-2010, 2010.

Warneke, C., Schwarz, J. P., Dibb, J., Kalashnikova, O., Frost, G., Al-Saad, J., Brown, S. S., Brewer, W. A., Soja, A., Seidel, F. C., Washenfelder, R. A., Wiggins, E. B., Moore, R. H., Anderson, B. E., Jordan, C., Yacovitch, T. I., Herndon, S. C., Liu, S., Kuwayama, T., Jaffe, D., Johnston, N., Selimovic, V., Yokelson, R., Giles, D. M., Holben, B. N., Goloub, P., Popovici, I., Trainer, M., Kumar, A., Pierce, R. B., Fahey, D., Roberts, J., Gargulinski, E. M., Peterson, D. A., Ye, X. X., Thapa, L. H., Saide, P. E., Fite, C. H., Holmes, C. D., Wang, S. Y., Coggon, M. M., Decker, Z. C. J., Stockwell, C. E., Xu, L., Gkatzelis, G., Aikin, K., Lefer, B., Kaspari, J., Griffin, D., Zeng, L. H., Weber, R., Hastings, M., Chai, J. J., Wolfe, G. M., Hanisco, T. F., Liao, J., Jost, P. C., Guo, H. Y., Jimenez, J. L., Crawford, J., and Team, F.-A. S.: Fire Influence on Regional to Global Environments and Air Quality (FIREX-AQ), Journal of Geophysical Research, 128, e2022JD037758, 10.1029/2022JD037758, 2023.

Worden, J., Saatchi, S., Keller, M., Bloom, A. A., Liu, J., Parazoo, N., Fisher, J. B., Bowman, K., Reager, J. T., Fahy, K., Schimel, D., Fu, R., Worden, S., Yin, Y., Gentine, P., Konings, A. G., Quetin, G. R., Williams, M., Worden, H., Shi, M. J., and Barkhordarian, A.: Satellite Observations of the Tropical Terrestrial Carbon Balance and Interactions With the Water Cycle During the 21st Century, Rev Geophys, 59, e2020RG000711, 10.1029/2020RG000711, 2021.

Wu, K., Yang, X. Y., Chen, D., Gu, S., Lu, Y. Q., Jiang, Q., Wang, K., Ou, Y. H., Qian, Y., Shao, P., and Lu, S. H.: Estimation of biogenic VOC emissions and their corresponding impact on ozone and secondary organic aerosol formation in China, Atmos Res, 231, 104656, 10.1016/j.atmosres.2019.104656, 2020.

Xie, X., Wang, T., Yue, X., Li, S., Zhuang, B., Wang, M., and Yang, X.: Numerical modeling of ozone damage to plants and its effects on atmospheric CO2 in China, Atmospheric Environment, 217, 116970, 10.1016/j.atmosenv.2019.116970, 2019.

Yuan, W. P., Liu, S. G., Yu, G. R., Bonnefond, J. M., Chen, J. Q., Davis, K., Desai, A. R., Goldstein, A. H., Gianelle, D., Rossi, F., Suyker, A. E., and Verma, S. B.: Global estimates of evapotranspiration and gross primary production based on MODIS and global meteorology data, Remote Sensing of Environment, 114, 1416-1431, 2010.

Yuan, X. Y., Calatayud, V., Gao, F., Fares, S., Paoletti, E., Tian, Y., and Feng, Z. Z.: Interaction of drought and ozone exposure on isoprene emission from extensively cultivated poplar, Plant Cell Environ, 39, 2276-2287, 10.1111/pce.12798, 2016.

Yue, X., and Unger, N.: Ozone vegetation damage effects on gross primary productivity in the United States, Atmospheric Chemistry and Physics, 14, 9137-9153, 10.5194/acp-14-9137-2014, 2014.

Yue, X., and Unger, N.: The Yale Interactive terrestrial Biosphere model version 1.0: description, evaluation and implementation into NASA GISS ModelE2, Geosci Model Dev, 8, 2399-2417, 10.5194/gmd-8-2399-2015, 2015.

Yue, X., Unger, N., Keenan, T. F., Zhang, X., and Vogel, C. S.: Probing the past 30-year phenology trend of U.S. deciduous forests, Biogeosciences, 12, 4693-4709, 10.5194/bg-12-4693-2015, 2015.

Yue, X., Keenan, T. F., Munger, W., and Unger, N.: Limited effect of ozone reductions on the 20-year photosynthesis trend at Harvard forest, Global Change Biology, 22, 3750-3759, 10.1111/gcb.13300, 2016.

Yue, X., and Unger, N.: Aerosol optical depth thresholds as a tool to assess diffuse radiation fertilization of the land carbon uptake in China, Atmospheric Chemistry and Physics, 17, 1329-1342, 10.5194/acp-17-1329-2017, 2017.

Yue, X., Unger, N., Harper, K., Xia, X., Liao, H., Zhu, T., Xiao, J., Feng, Z., and Li, J.: Ozone and haze pollution weakens net primary productivity in China, Atmospheric Chemistry and Physics, 17, 6073-6089, 10.5194/acp-17-6073-2017, 2017.

Yue, X., and Unger, N.: Fire air pollution reduces global terrestrial productivity, Nature Communications, 9, 5413, 10.1038/s41467-018-07921-4, 2018.

Yue, X., Zhang, T., and Shao, C.: Afforestation increases ecosystem productivity and carbon storage in China during the 2000s, Agricultural and Forest Meteorology, 296, 108227, 10.1016/j.agrformet.2020.108227, 2021.

Zhang, Y., Li, C., Trettin, C. C., Li, H., and Sun, G.: An integrated model of soil, hydrology, and vegetation for carbon dynamics in wetland ecosystems, Global Biogeochemical Cycles, 16, 9-1-9-17, https://doi.org/10.1029/2001GB001838, 2002.

Zhang, Z., Zimmermann, N. E., Stenke, A., Li, X., Hodson, E. L., Zhu, G. F., Huang, C. L., and Poulter, B.: Emerging role of wetland methane emissions in driving 21st century climate change, P Natl Acad Sci USA, 114, 9647-9652, 10.1073/pnas.1618765114, 2017.

Zhang, Z., Fluet-Chouinard, E., Jensen, K., McDonald, K., Hugelius, G., Gumbricht, T., Carroll, M., Prigent, C., Bartsch, A., and Poulter, B.: Development of the global dataset of Wetland Area and Dynamics for Methane Modeling (WAD2M), Earth System Science Data, 13, 2001-2023, 10.5194/essd-13-2001-2021, 2021.

Zhu, Q., Liu, J., Peng, C., Chen, H., Fang, X., Jiang, H., Yang, G., Zhu, D., Wang, W., and Zhou, X.: Modelling methane emissions from natural wetlands by development and application of the TRIPLEX-GHG model, Geosci Model Dev, 7, 981-999, 10.5194/gmd-7-981-2014, 2014.

Zhuang, Q., Melillo, J. M., Kicklighter, D. W., Prinn, R. G., McGuire, A. D., Steudler, P. A., Felzer, B. S., and Hu, S.: Methane fluxes between terrestrial ecosystems and the atmosphere at northern high latitudes during the past century: A retrospective analysis with a process-based biogeochemistry model, Global Biogeochem Cy, 18, GB3010, 10.1029/2004GB002239, 2004.

1181
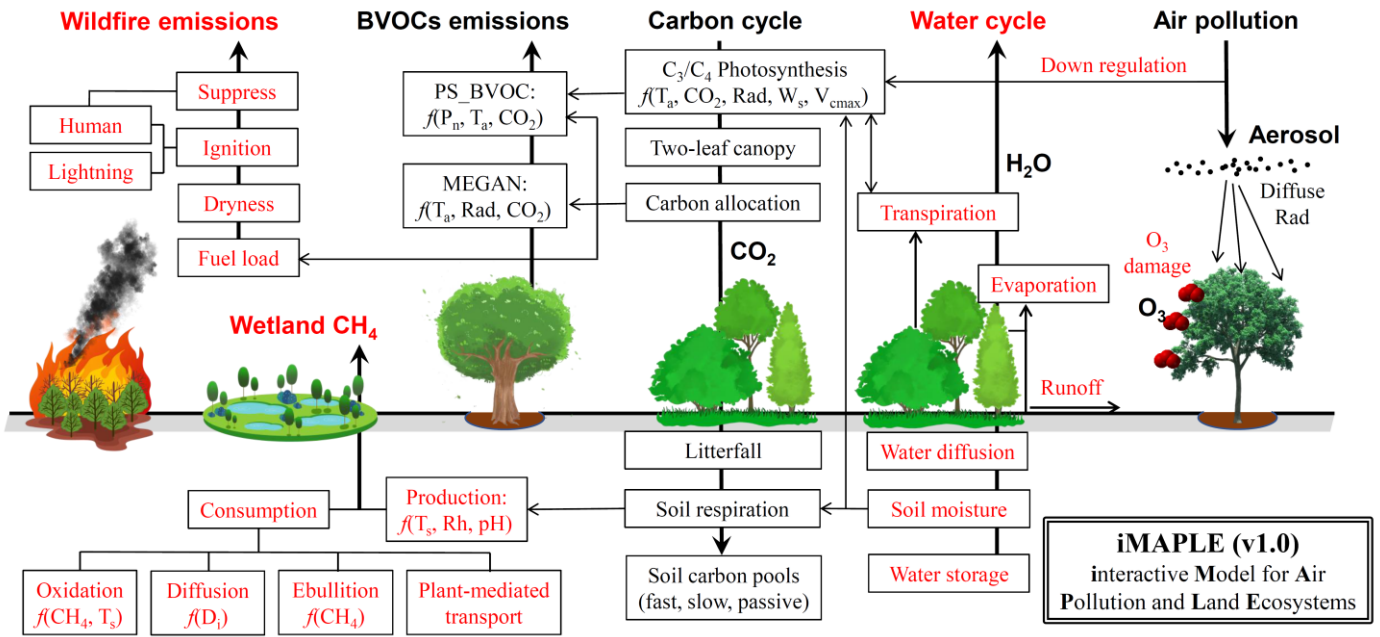
1183 **Figure 1** The illustration of biogeochemical processes in the iMAPLE version 1.0
1184 model. The carbon cycle is connected with water cycle, wildfire emissions, biogenic
1185 volatile organic compounds (BVOCs) emissions, wetland methane emissions, and is
1186 affected by air pollutants including aerosols and ozone. The bold arrows indicate the
1187 directions of fluxes and air pollutants. The thin arrows indicate the influential pathways
1188 among different components. The dependences on key parameters are shown for some
1189 processes. Red fonts indicate new or updated processes in iMAPLE relative to the YIBs
1190 model. For detailed parameterizations please refer to section 2.2.

1191

1192

1193
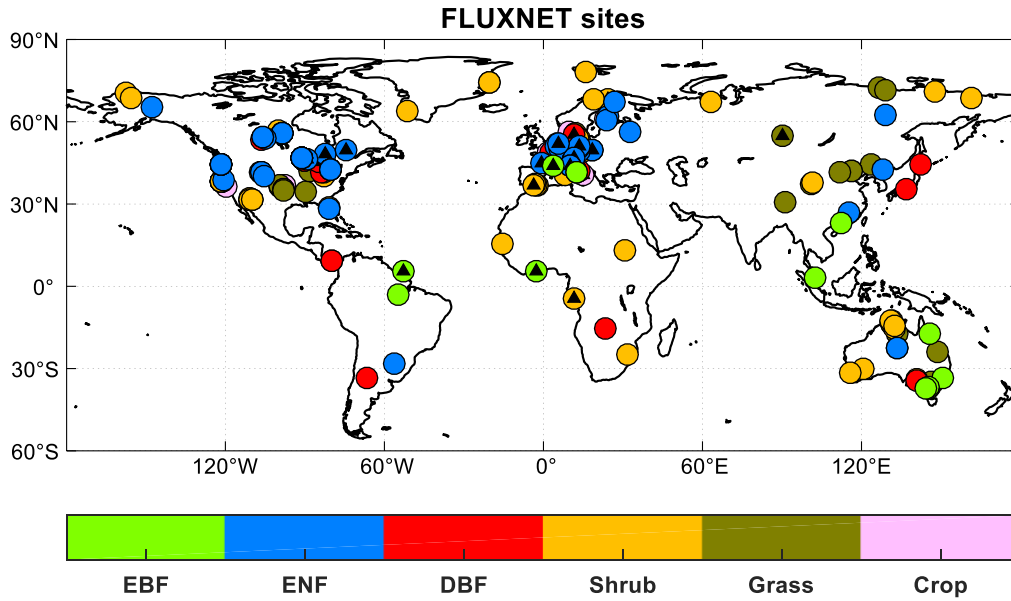
**Figure 2** Spatial distributions of 201 sites from global FLUXNET network. The colors indicate various plant functional types (PFTs) including evergreen broadleaf forest (EBF, 13 sites), evergreen needleleaf forest (ENF, 57 sites), deciduous broadleaf forest (DBF, 25 sites), Shrub (52 sites), Grass (37 sites), and Crop (17 sites). The black triangles indicate sites with at least one-year observations of diffuse radiation.
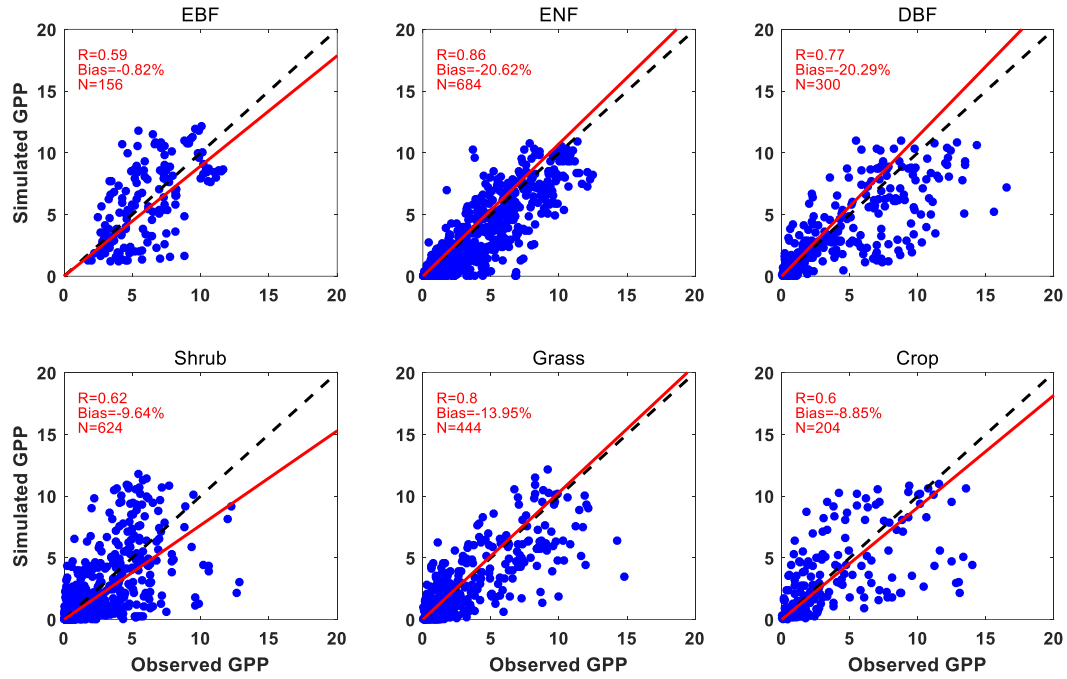
1202

1203    **Figure 3** Comparisons between observed and simulated monthly GPP from 201 FLUXNET sites.
1204    Each point indicates the average value of one month at a site. The red line represents linear
1205    regression between observations and simulations from the BASE experiment. The correlation
1206    coefficient (R), normalized mean bias and numbers of points/months (N) are shown on each panel.
1207    The comparisons are grouped into six PFTs including EBF, ENF, DBF, Shrub, Grass, and Crop. The
1208    unit is g C m$^{-2}$ day$^{-1}$.

1209
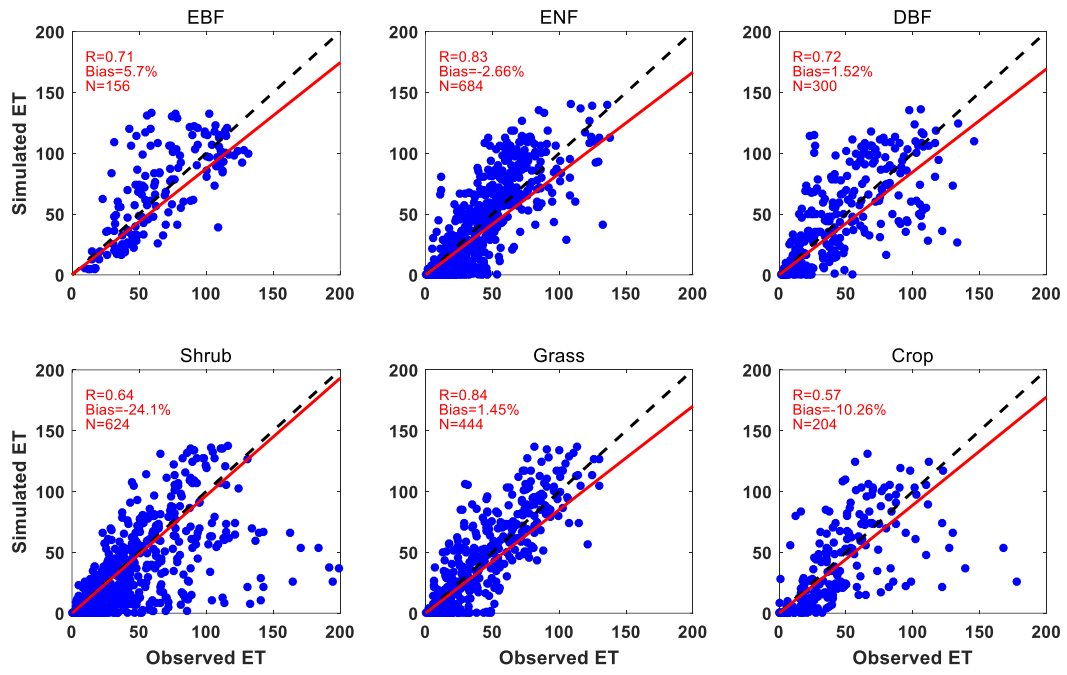
1210

1211 **Figure 4** The same as Figure 3 but for ET. The unit is mm month$^{-1}$.

1212

1213
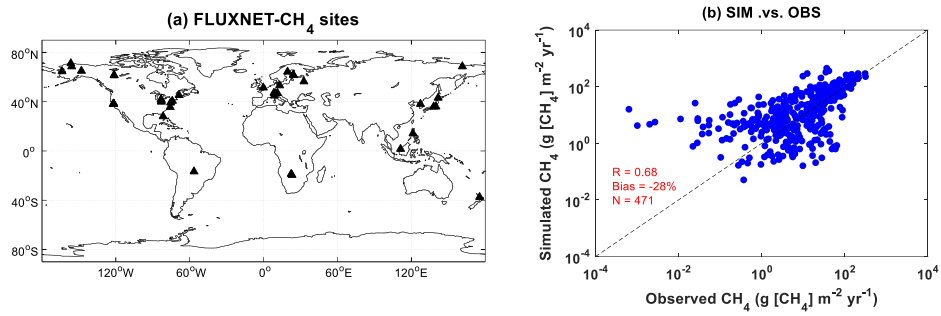
1214

**Figure 5** (a) Spatial distribution of global FLUXNET-CH$_4$ sites and (b) comparisons between observed and simulated monthly methane flux from the BASE experiment. Filled triangles indicate sites with at least six months observations of wetland CH$_4$ fluxes. Each point represents average value of monthly methane emission at one site. The correlation coefficient (R), normalized mean bias and numbers of points/months (N) are shown on the right panel. The unit is g [CH$_4$] m$^{-2}$ yr$^{-1}$.

1215
1216
1217
1218
1219
1220
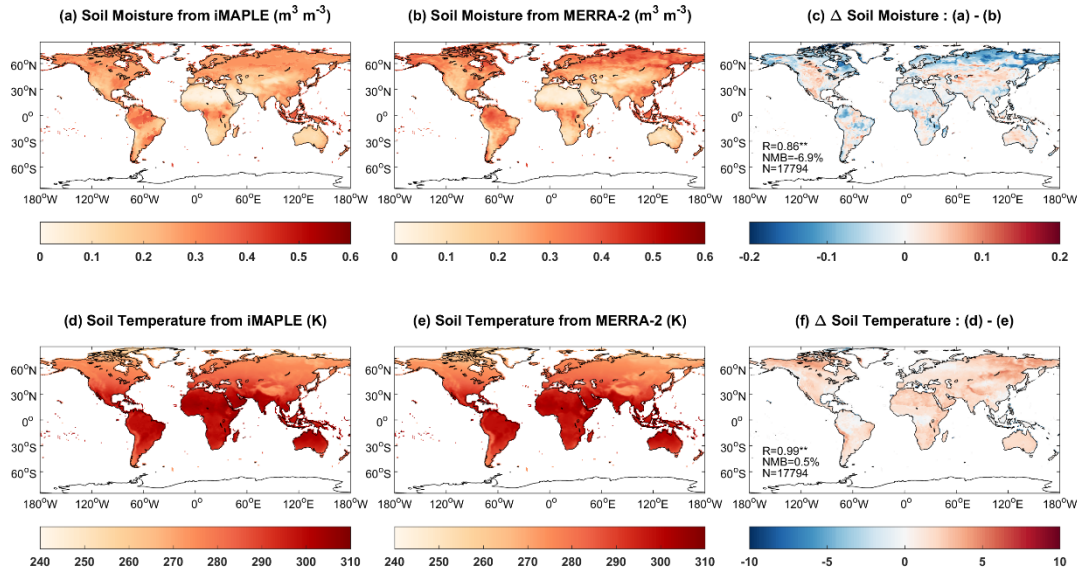
1221

**Figure 6** Comparisons of simulated (a) soil moisture (m³ m⁻³) and (d) soil temperature (K) from the
iMAPLE model with (b, e) the MERRA-2 reanalyses. Both simulations from the BASE experiment
and observations from MERRA-2 reanalyses are averaged for the period of 1980-2020. The spatial
difference, correlation coefficient (R), normalized mean bias (NMB) between simulations and
observations and numbers of points (N) are shown on (c) and (f), respectively.

1227
1228
1229
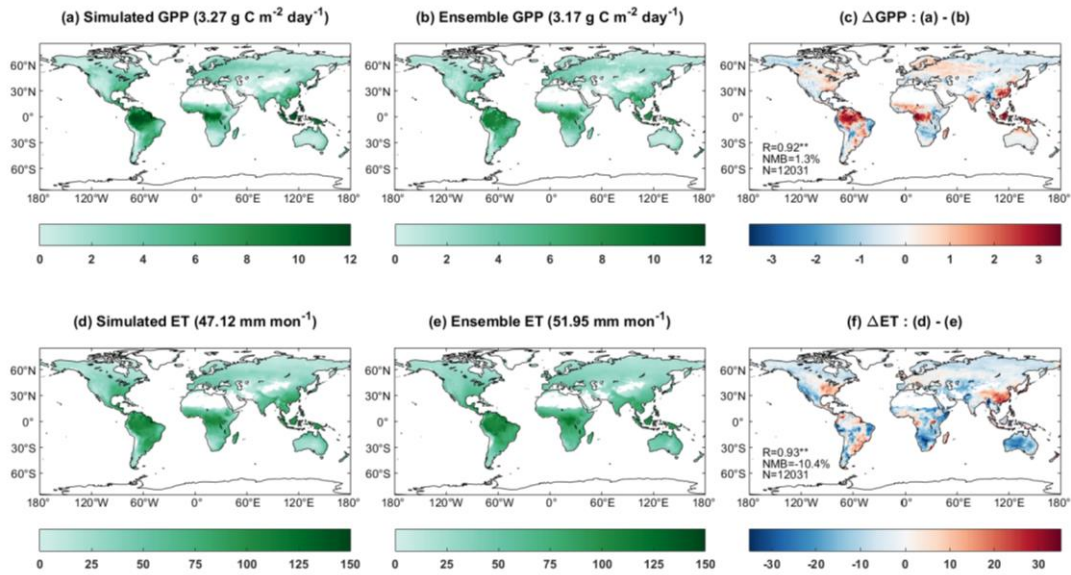
**Figure 7** Comparisons of simulated (a) gross primary productivity (GPP, g C m$^{-2}$ day$^{-1}$) and (d) evapotranspiration (ET, mm month$^{-1}$) with ensemble products from (b, e) observations. Simulated GPP and ET are performed by iMAPLE driven with meteorology from MERRA-2 reanalysis (BASE) during 2001-2013. Ensemble GPP products are from the average values of SIF-based GOSIF and satellite-based GLASS GPP products. Ensemble ET products include FLUXCOM and GLASS products during 2001-2013. The spatial difference, correlation coefficient (R), normalized mean bias (NMB) between simulations and observations and numbers of points (N) are shown on (c) and (f). Only land grids with vegetation are shown on each panel, and their area-weighed values are shown in titles.

1241
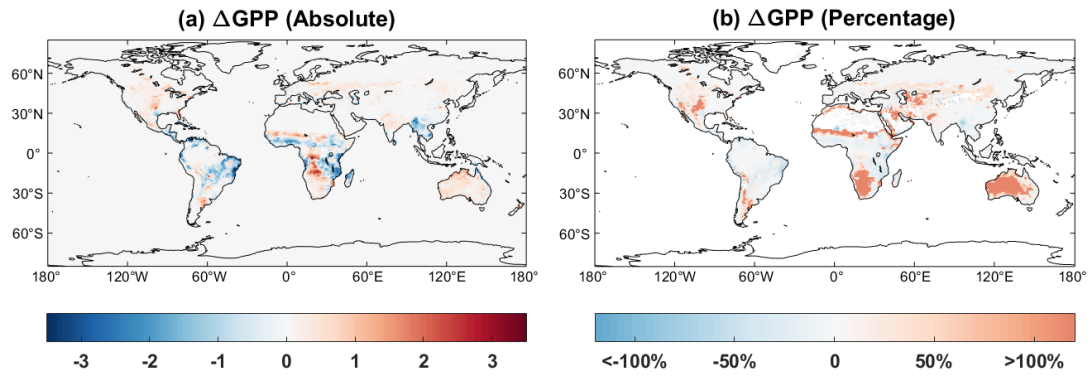
1242 **Figure 8** Absolute (g C m⁻² day⁻¹) and relative (%) differences of global GPP between simulations

1243 with (BASE) and without (BASE_NW) two-way carbon-water coupling processes. Simulation

1244 results are averaged for the period of 1980-2020.

1245
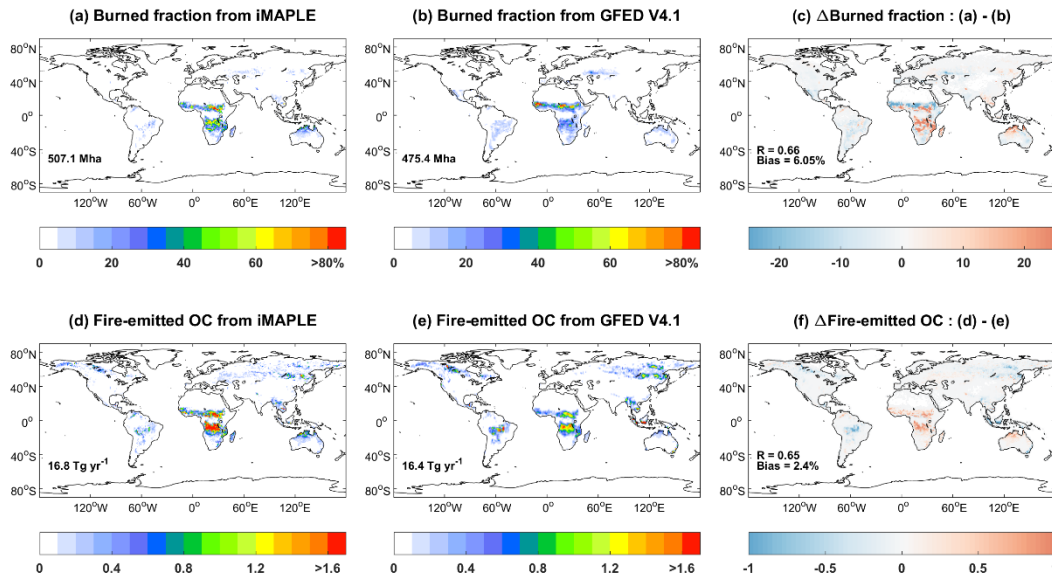
1246

**Figure 9** Comparisons of global burned fraction (%) and fire-emitted OC emissions ($10^{-3}$ kg km$^{-1}$ yr$^{-1}$) between (a, d) simulations and (b, e) observations. Simulations are performed using iMAPLE and observations are from GFED V4.1 fire emissions products. Both simulations from the BASE experiment and observations are averaged for the 1997-2016 period. The global total area burned are shown on (a) and (b), and total OC emissions are shown on (d) and (e). The spatial difference, correlation coefficient (R), and normalized mean biases between simulations and observations are shown on (c) and (f).

1254
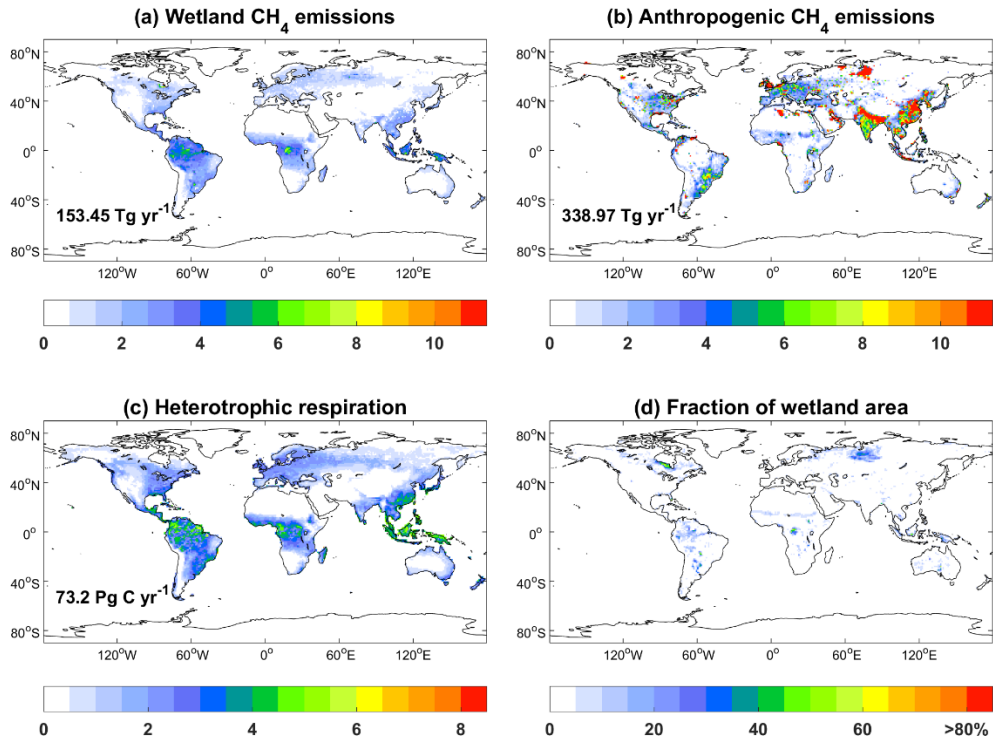
Figure 10 Global simulated CH$_4$ emissions (g [CH4] m$^{-2}$ yr$^{-1}$) from (a) wetland and (b) anthropogenic sources, (c) heterotrophic respiration (gC m$^{-2}$ day$^{-1}$) and (d) fraction of wetland area. The simulations are from the BASE experiment. Anthropogenic sources are adopted from CMIP6 including the sectors of energy, agriculture, industrial, residential, shipping, solvent and transportation. The global total emissions and heterotrophic respirations are shown on each panel. All variables are averaged for 2000-2014.
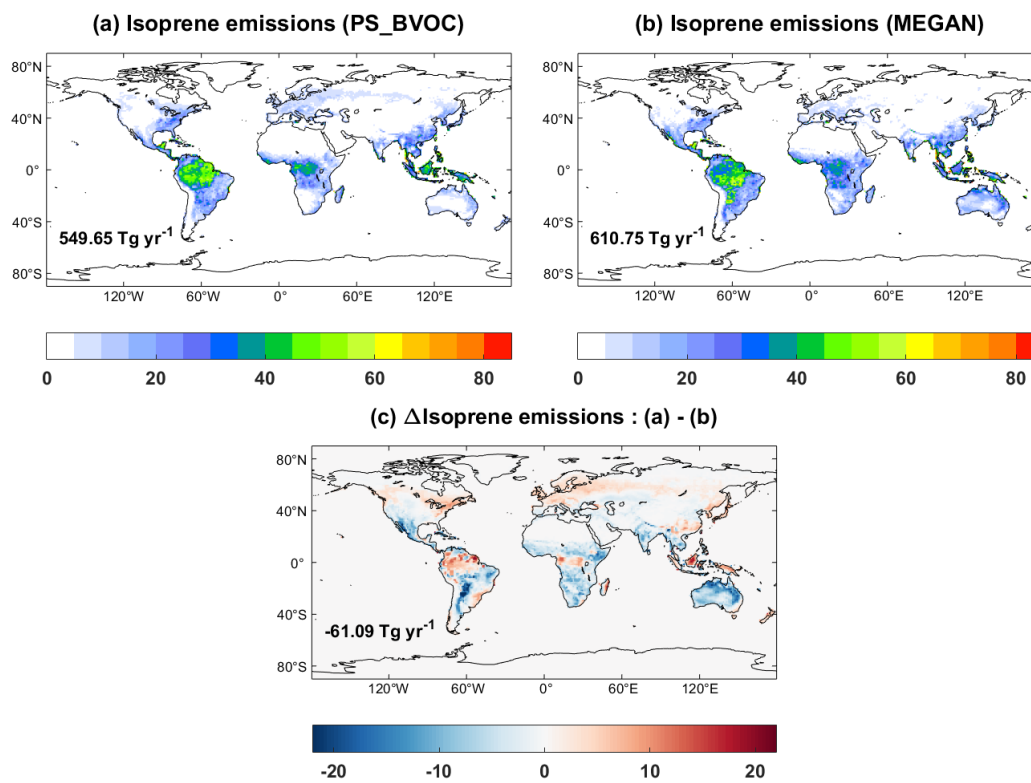
1263

1264 **Figure 11** Global isoprene emissions (mg C m$^{-2}$ day$^{-1}$) from (a) MEGAN, (b) PS_BVOC schemes

1265 and (c) their differences during 1980-2020. The simulations are from the BASE experiment. The

1266 global total emissions are shown on each panel.

1267
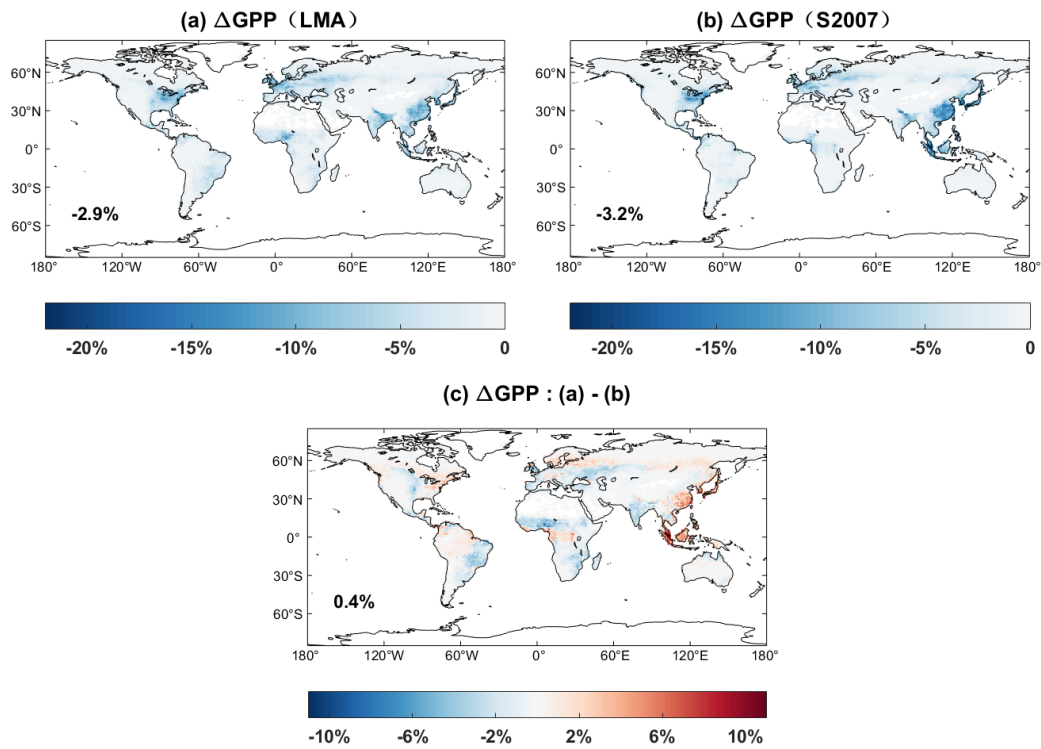
1268

**Figure 12** Percentage changes of global GPP caused by ozone damage effects based on (a) LMA
(O3LMA – BASE) and (b) S2007 (O3S2007 – BASE) schemes. The ozone damage schemes include
(a) trait leaf mass per area (LMA)-based from the O3LMA experiment, (b) S2007 plant ozone
sensitivity from the O3S2007 experiment and (c) their differences.
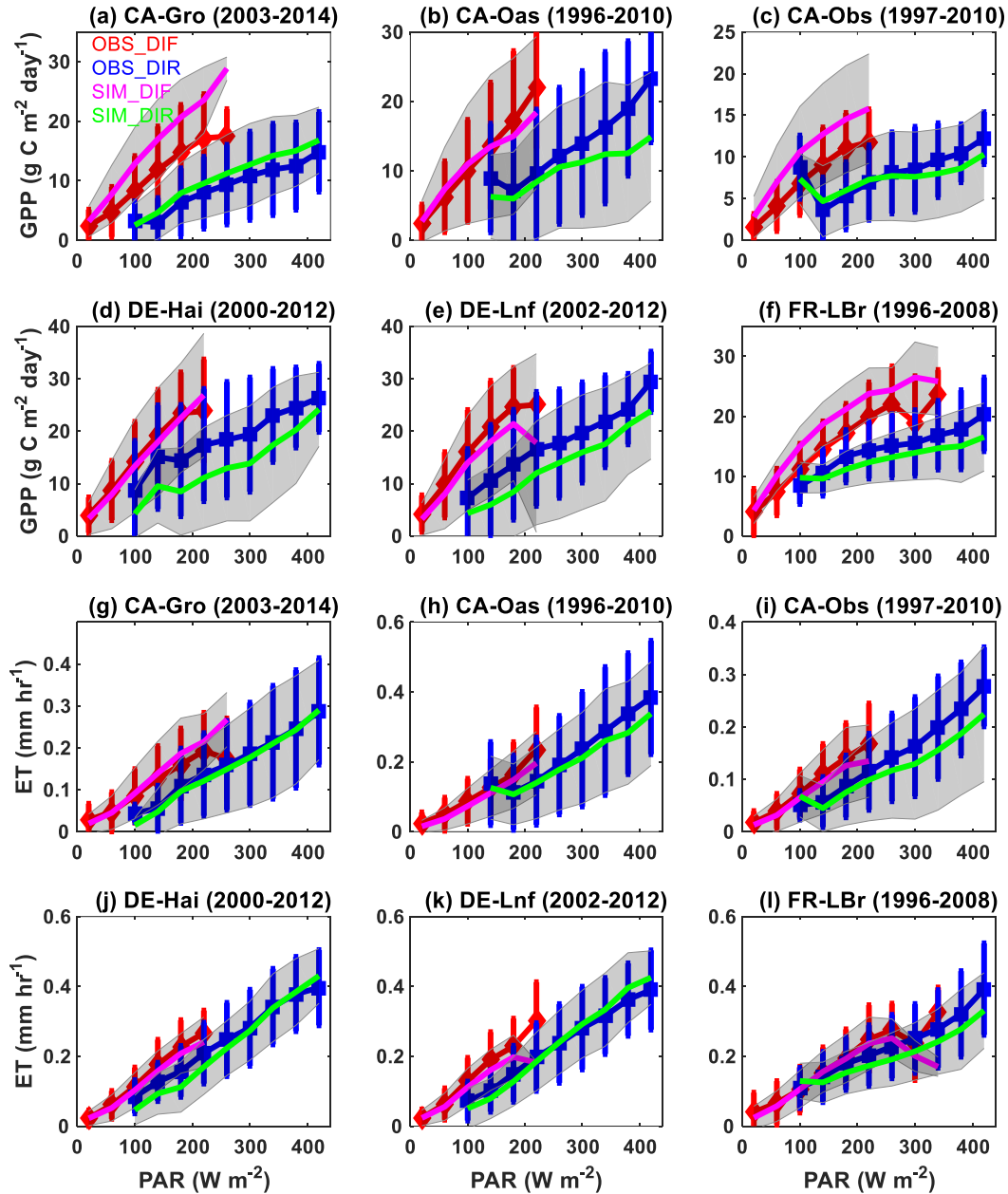
1269
1270
1271
1272
1273
1274
1275

**Figure 13** Observed and simulated responses of site-level (a-f) GPP and (g-l) ET to diffuse and direct radiation at the FLUXNET sites. Photosynthetically active radiation (PAR) reaching the surface are divided into diffuse (diffuse fraction > 0.75) and direct (diffuse fraction < 0.25) radiation at six FLUXNET sites with more than 10 years of observations. Observations (simulations) are grouped over PAR bins of 40 W m$^{-2}$ with errorbars (shadings) indicating standard deviations of GPP and ET for each bin. The red (blue) and magenta (green) represent observed and simulated responses of GPP and ET to diffuse (direct) radiation. Units of GPP and ET are g C m$^{-2}$ day$^{-1}$ and mm hr$^{-1}$, respectively.